NAVAL POSTGRADUATE SCHOOL

MONTEREY, CALIFORNIA

THESIS

MICROWAVE DETECTION WITH SINGLE-BAND METAMATERIALS FOR HIGH POWER MICROWAVE WEAPONS

by

Edward V. Wulff

December 2017

Thesis Advisor:	Dragoslav Grbovic
Second Reader:	Fabio Alves

Approved for public release. Distribution is unlimited.

THIS PAGE INTENTIONALLY LEFT BLANK

REPORT DOCUMENTATION PAGE			Form Approved OMB No. 0704-0188

Public reporting burden for this collection of information is estimated to average 1 hour per response, including the time for reviewing instruction, searching existing data sources, gathering and maintaining the data needed, and completing and reviewing the collection of information. Send comments regarding this burden estimate or any other aspect of this collection of information, including suggestions for reducing this burden, to Washington headquarters Services, Directorate for Information Operations and Reports, 1215 Jefferson Davis Highway, Suite 1204, Arlington, VA 22202-4302, and to the Office of Management and Budget, Paperwork Reduction Project (0704-0188) Washington, DC 20503.

1. AGENCY USE ONLY *(Leave blank)*	2. REPORT DATE December 2017	3. REPORT TYPE AND DATES COVERED Master's thesis

4. TITLE AND SUBTITLE MICROWAVE DETECTION WITH SINGLE-BAND METAMATERIALS FOR HIGH POWER MICROWAVE WEAPONS	5. FUNDING NUMBERS
6. AUTHOR(S) Edward V. Wulff	
7. PERFORMING ORGANIZATION NAME(S) AND ADDRESS(ES) Naval Postgraduate School Monterey, CA 93943-5000	8. PERFORMING ORGANIZATION REPORT NUMBER
9. SPONSORING /MONITORING AGENCY NAME(S) AND ADDRESS(ES) Office of Naval Research 875 N Randolph St, Arlington, VA 22217	10. SPONSORING / MONITORING AGENCY REPORT NUMBER N0001416WX01128

11. SUPPLEMENTARY NOTES The views expressed in this thesis are those of the author and do not reflect the official policy or position of the Department of Defense or the U.S. Government. IRB number ____N/A____.

12a. DISTRIBUTION / AVAILABILITY STATEMENT Approved for public release. Distribution is unlimited.	12b. DISTRIBUTION CODE

13. ABSTRACT (maximum 200 words)

As the development of high power microwaves (HPM) continues, the potential threat to electronic systems increases. The use of metamaterials' (MM) unique characteristics has the capability to be a countermeasure against HPM weapons as shielding for electronic systems. This thesis continues to explore the use of MMs as a countermeasure by studying the integration of field effect transistors (FET) with metal/ dielectric/metal MM as a method of detection. The effects on the MM absorption profile were examined with the integration of FETs. The behavior of the FETs was also examined at the MM resonant frequency. Finite element simulations and experiments, which introduced electromagnetic (E&M) fields onto the MM board, were used to conduct the analysis. Simulations demonstrated that FETs have the potential to shift the resonant frequency to the left and generate an electric potential at the resonant frequency. The experimental board resonant frequency did not shift due to the limited number of FETs on the board. We conclude that further work for MM board detection of HPM weapons, with exposure of MM boards to megawatt radiation of higher frequency, is required.

14. SUBJECT TERMS metamaterial, microwave, high power microwave weapon, directed energy weapon, absorber, unit cells, shielding, FET, detection	15. NUMBER OF PAGES 69
	16. PRICE CODE

17. SECURITY CLASSIFICATION OF REPORT	18. SECURITY CLASSIFICATION OF THIS PAGE	19. SECURITY CLASSIFICATION OF ABSTRACT	20. LIMITATION OF ABSTRACT
Unclassified	Unclassified	Unclassified	UU

NSN 7540-01-280-5500 Standard Form 298 (Rev. 2-89) Prescribed by ANSI Std. 239-18

THIS PAGE INTENTIONALLY LEFT BLANK

Approved for public release. Distribution is unlimited.

MICROWAVE DETECTION WITH SINGLE-BAND METAMATERIALS FOR HIGH POWER MICROWAVE WEAPONS

Edward V. Wulff
Lieutenant, United States Navy
B.S., Oregon State University, 2011

Submitted in partial fulfillment of the
requirements for the degree of

MASTER OF SCIENCE IN APPLIED PHYSICS

from the

NAVAL POSTGRADUATE SCHOOL
December 2017

Approved by: Dragoslav Grbovic
Thesis Advisor

Fabio Alves
Second Reader

Kevin B. Smith
Chair, Department of Physics

THIS PAGE INTENTIONALLY LEFT BLANK

ABSTRACT

As the development of high power microwaves (HPM) continues, the potential threat to electronic systems increases. The use of metamaterials' (MM) unique characteristics has the capability to be a countermeasure against HPM weapons as shielding for electronic systems. This thesis continues to explore the use of MMs as a countermeasure by studying the integration of field effect transistors (FET) with metal/dielectric/metal MM as a method of detection. The effects on the MM absorption profile were examined with the integration of FETs. The behavior of the FETs was also examined at the MM resonant frequency. Finite element simulations and experiments, which introduced electromagnetic (E&M) fields onto the MM board, were used to conduct the analysis. Simulations demonstrated that FETs have the potential to shift the resonant frequency to the left and generate an electric potential at the resonant frequency. The experimental board resonant frequency did not shift due to the limited number of FETs on the board. We conclude that further work for MM board detection of HPM weapons, with exposure of MM boards to megawatt radiation of higher frequency, is required.

THIS PAGE INTENTIONALLY LEFT BLANK

TABLE OF CONTENTS

I. INTRODUCTION 1

II. OVERVIEWS 3
- A. HIGH POWER MICROWAVE WEAPONS OVERVIEW 3
- B. METAMATERIALS OVERVIEW 5
- C. ENHANCEMENT NMOSFET OVERVIEW 8

III. METAMATERIAL BOARD DESIGN 13

IV. EXPERIMENTAL SETUP 17
- A. MODELING 17
- B. CHARACTERIZATION SETUP 21
- C. SENSING CHARACTERIZATION SETUP 23

V. RESULTS 25
- A. ABSORPTION RESULTS 25
- B. SENSING RESULTS 27
- C. PROBE POSITION ANALYSIS 30

VI. CONCLUSION 33
- A. RESULTS SUMMARY 33
- B. FUTURE WORK 34
  - 1. Probe Voltage Amplification 34
  - 2. COMSOL Simulation Improvements 36
- C. FINAL THOUGHTS 37

APPENDIX A. MATLAB CODE 39

APPENDIX B. METAMATERIAL CURVITURE 41

APPENDIX C. ADDITIONAL COMSOL MODEL IMAGES 43

APPENDIX D. SWEEP OSCILLATOR NOTE 47

LIST OF REFERENCES 49

INITIAL DISTRIBUTION LIST 53

THIS PAGE INTENTIONALLY LEFT BLANK

LIST OF FIGURES

Figure 1. Top Level Block Diagram of an HPM Weapon. Adapted from [10]. 3

Figure 2. First Realized MM Board with Negative Permittivity and Permeability. Source: [14]. 5

Figure 3. Permittivity and Permeability Regions. Source: [18]. 6

Figure 4. How a Wave Bends Based on Permittivity and Permeability. Adapted from [19].....7

Figure 5. (a) MMA Unit Cell Examples. Sources: [20], [23]. (b) Generic MMA Unit Cell. Adapted from [5], [6]. (c) Generic Cross-Sectional Area MMA Sketch. 8

Figure 6. (a) Block Diagram of an FET. (b) NMOSFET Circuit Drawing. Adapted from [25].....9

Figure 7. NMOSFET Design Sketch. Adapted from [25].....10

Figure 8. NMOSFET Regions of Operation. Source: [26].....11

Figure 9. Resonant Frequency vs. Inverse Resonant Square Length. Adapted from [5]. 13

Figure 10. (a) Seven mm MM Board with FETs. (b) Sketch of the Cross-Sectional Area a Unit Cell. 14

Figure 11. (a) SEM Micrograph of the Cross-Sectional Area with FET Probe. (b) FET Circuit Sketch with MM. (c) 2-D Sketch of MM Board Cross Section with FETs.....15

Figure 12. (a) 2-D Sketch of Seven mm COMSOL Model. (b) 2-D Sketch of Seven mm Unit COMSOL Model with Probe Inserted. 17

Figure 13. 2-D Port and Boundary Diagram. Adapted from [5]. 18

Figure 14. Lumped Port Diagram. Adapted from [28].....20

Figure 15. SPICE Simulation Model.....21

Figure 16. Absorption Apparatus Block Diagram and Experimental Setup. 22

Figure 17. (a) Wire Soldering onto MM Board. (b) MM Board Hooked up to Device Analyzer.....23

Figure 18. Mirror and MM Board Reflection Data. 25

Figure 19. MM Board Simulation and Experimental Absorption. 26

Figure 20. Experimental Absorption with Different Resonator Square Sizes. 27

Figure 21. Simulation Electric Potential Magnitude and Phase. 28

Figure 22. Normalized Absorption and Electric Potential from COMSOL Simulations 29

Figure 23. Spice Simulation FET Model.....30

Figure 24. Simulated Absorption at Varying Probe Heights.....31

Figure 25. Simulated Electric Potential Magnitude and Phase at Varying Probe Heights. 32

Figure 26. (a) Current MM Board Layout. (b) Proposed MM Board Layout. 34

Figure 27. Example of Circuit for MM Board Sensing. 36

Figure 28. Seven mm COMSOL Unit Cell Model.....43

Figure 29. Seven mm COMSOL Unit Cell with Probe and Lumped Port Model 44

Figure 30. Enlarged Picture of the Probe in Figure 29.....45

LIST OF ACRONYMS AND ABBREVIATIONS

2-D	2 dimensional
cm	Centimeter
DC	Direct Current
E&M	Electromagnetic
FET	Field Effect Transistor
GHz	Gigahertz
HPM	High Power Microwave
I-V	Current and Voltage
MHz	Megahertz
mm	Millimeter
MM	Metamaterial
MMA	Metamaterial Absorber
mW	Milliwatts
NMOSFET	N-type Metal Oxide Semiconductor Field Effect Transistor
NPS	Naval Postgraduate School
ONR	Office of Naval Research
OPAMP	Operational Amplifier
PCB	Printed Circuit Board
PEC	Perfect Electrical Conductor
PMC	Perfect Magnetic Conductor
µm	Micrometer
µW	Microwatt
V_{ds}	Drain-to-Source Voltage
V_{gs}	Gate-to-Source Voltage
V_{rms}	RMS Voltage
V_{th}	Threshold Voltage

THIS PAGE INTENTIONALLY LEFT BLANK

ACKNOWLEDGMENTS

The research conducted in this thesis is sponsored under contract N0001416WX01128 by the Office of Naval Research.

I would like to thank Robert Broadston from the Electrical and Computer Engineering Department of the Naval Postgraduate School for providing technical support with testing equipment. I would also like to thank Richard Mattish, who assisted with thesis research during his 2017 summer NREIP internship at NPS.

THIS PAGE INTENTIONALLY LEFT BLANK

I. INTRODUCTION

With the continued optimization, miniaturization and cost reduction of electronic components, the vulnerability of electronic systems against electromagnetic (E&M) waves in the microwave regime have significantly increased [1]. To exploit this vulnerability, research of high power microwave (HPM) weapons have increased not only in the United States but within many foreign nations [2]. Within the last 15 years, several nations have made advancements and proposed designs for HPM weapons that can become potential threats. In 2002 the Russian government began marketing the development of the RANET-E to foreign countries, a mobile HPM weapon against air contacts with a proposed effective range of 13 km [3]. In January 2017, a Chinese scientist was awarded for the development of an HPM weapon that would fit onto their naval vessels for anti-ship missile defense [4].

With the increased interest of HPM weapons, shielding methods need to be investigated as a countermeasure for electronic systems. One potential method of shielding electronic systems is to utilize metamaterials (MM), designed to absorb frequencies in the microwave regime. In addition to absorbing the energy of the incoming radiation, the MM structures can have an effect of cross-section reduction. Previous research has demonstrated the capability to absorb single-band frequencies [5] as well as multiple-band frequencies [6] using relatively simple MM structures. This thesis presents an attempt to expand on the subject by examining a potential method of detection for incoming radiation with a MM board integrated with field effect transistors (FET). By analyzing incoming radiation, the capability to detect and classify a HPM weapon is possible, based on resonant frequency and generated current in the FET. The objectives of this thesis would be to

- characterize the absorption profile of a MM board with FETs;
- simulate the electric potential applied to an FET at the resonant frequency of the MM board; and
- experimentally measure the electrical potential applied to the FET.

THIS PAGE INTENTIONALLY LEFT BLANK

II. OVERVIEWS

A. HIGH POWER MICROWAVE WEAPONS OVERVIEW

HPM Weapons are one of the three types of directed energy weapons, the other two being high-energy lasers and charged-particle beams [7]. To be classified as a HPM weapon, it must have a minimum output peak power of 100 megawatts and be within the frequency range of 1 to 100 Gigahertz (GHz) [1]. One of the first historical ideas of an HPM weapon occurred in the 1930s with the British government. During this time, the British air ministry knew of the potential threat of German bombers conducting air raids in Britain's air space. In response to this threat, they asked the British National Physical Laboratory the feasibility to shoot down aircrafts and incapacitate crews with electromagnetic radiation [8]. While today's weapons may not fit exactly what the British air ministry wanted, current HPM weapons have the potential for multiple missions, such as personnel deterrence [9] and air defense systems [1].

A HPM Weapon can be represented as three top-level system blocks in a block diagram, as seen in Figure 1 [10]. The system starts with the power source as the input and ends with the transmission of the wave as the output. The pulse power generator takes the power provided by the source and creates a high-power signal in the chosen frequency range. The signal is then sent to the microwave converter to be converted into an E&M wave. The E&M wave is then directed and transmitted by the antenna to engage a target. The HPM weapons range of effectiveness is dependent on the peak power for the E&M wave and the size of the antenna utilized [2].

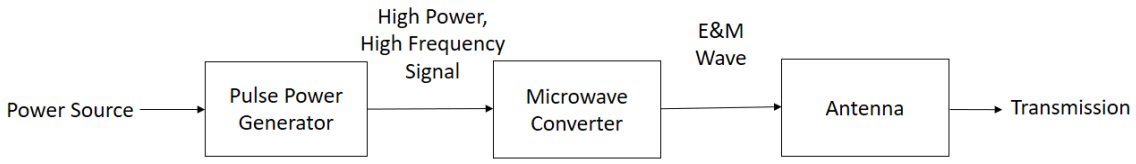

Figure 1. Top Level Block Diagram of an HPM Weapon. Adapted from [10].

Two types of HPM weapons are generally considered feasible, a narrowband and wideband weapon [10]. A narrowband weapon creates E&M waves within a small range of frequencies to engage a single target. A wideband weapon creates E&M waves in a wide range of frequencies to engage multiple targets but utilizes a lower peak power per frequency compared to the narrowband weapon. Knowledge of the target is required to exploit the frequency of greatest vulnerability with a narrowband weapon while no knowledge is required for wideband weapon.

There are two coupling paths for a HPM weapon to enter a system, front-door and back-door coupling [11]. Front-door coupling is the microwave signal using a direct path for entering a system to inflict damage to components and degrade a system. The direct path taken is through an antenna or sensor that is used to receive and transmit data. The systems targeted by this method generally interact with the external environment and have minimal shielding, as shielding would reduce their efficiency to operate [11]. Back-door coupling is the microwave signal using an indirect path to enter a targeted system to inflict damage. Examples of this include entering a gap created by pipes entering a shielded system or through the air vents of a computer.

The effect of a HPM weapon on an electronic system is dependent on the amount of power applied to the system. The two major types of damage classification are upset and burnout. An upset is when the system has a logic or memory issues that causes a temporary disruption in the system [1]. Burnout occurs when permanent damage is done to the electronics in the system [1]. The damage done in a burnout is caused thermally or by the electrical breakdown of the circuits [11].

HPM waves have numerous advantages that make them attractive for weapon applications. HPM weapons will operate while power is available. They are not limited by the storage of munitions and can be considered to have a “deep magazine” when compared to conventional weapons [1]. HPM waves are minimally affected by the weather, travels in space and have the capability to propagate at the speed of light. When an HPM weapon it utilized for an area attack, it will cause no physical damage to structures within the attack. The HPM weapons can also be used as non-lethal weapons against personnel threats, such as enemy soldiers [9].

B. METAMATERIALS OVERVIEW

MMs are man-made structures with unique electromagnetic properties not found in natural materials [12]. They were first theorized in the 1960s, with a study of the effects of a material having both a negative permittivity and permeability [13]. From there, one of the first experimental breakthroughs occurred in 2001, validating the theoretical study in the 1960s with split ring resonators and copper wires [14]; Figure 2. Today's MMs have the potential for multiple applications, examples including potential cloaking devices [15] and medical applications [16].

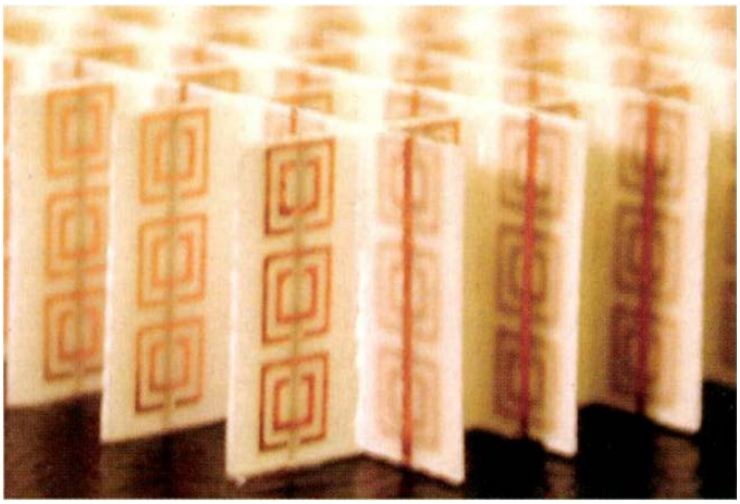

Figure 2. First Realized MM Board with Negative Permittivity and Permeability. Source: [14].

Typical MMs consist of a periodic layout of unit cells. Each unit cell has a metallic resonator that responds to a specific wavelength, or frequency [12]. Other factors that affect the resonant frequency include constituent properties, thickness of the materials layers and the spacing between unit cells [17]. The results of the design and material composition of MMs create a material with electromagnetic (E&M) properties different from the constituents, such as unique effective permittivity and permeability.

Permittivity, ε, and permeability, μ, are characteristics of a material that define how it interacts with an E&M waves, ε is related to the electric field and μ is related to

the magnetic field of the E&M wave. The materials found in nature have been identified to have either a positive ε and μ, a positive ε and negative μ or a negative ε and a positive μ [18]; Figure 3. MMs, however, have demonstrated an effective ε and μ that is negative [12].

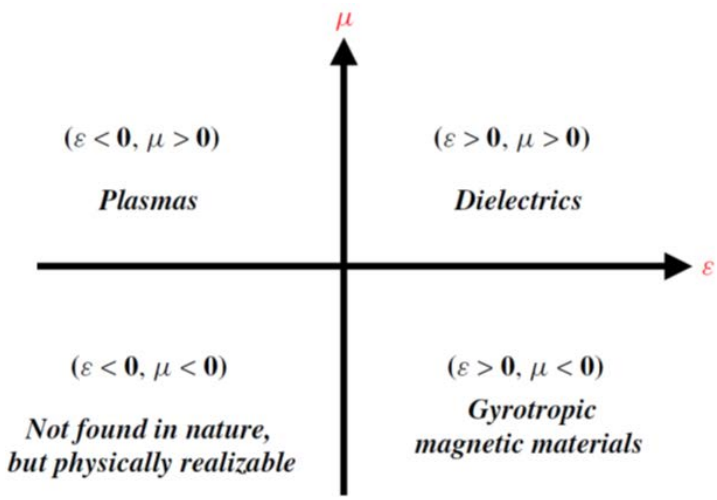

Figure 3. Permittivity and Permeability Regions. Source: [18].

One effect of having a negative ε and μ is creating an effective refractive index that is negative; Equation 1 [12].

$$n = -\sqrt{\varepsilon_r \mu_r} \tag{1}$$

This change affects how a wave bends when entering a new material as seen in Snell's Law; Equation 2.

$$n_1 \sin(\theta_1) = n_2 \sin(\theta_2) \tag{2}$$

Equation 2 can be rearranged to find θ_2; Equation 3.

$$\theta_2 = \sin^{-1}\left(\frac{n_1}{n_2}\sin[\theta_1]\right) \tag{3}$$

The negative refractive index results in a negative refracted angle, bending the wave opposite direction compared to a material with a positive ε and μ [19], as seen in Figure 4.

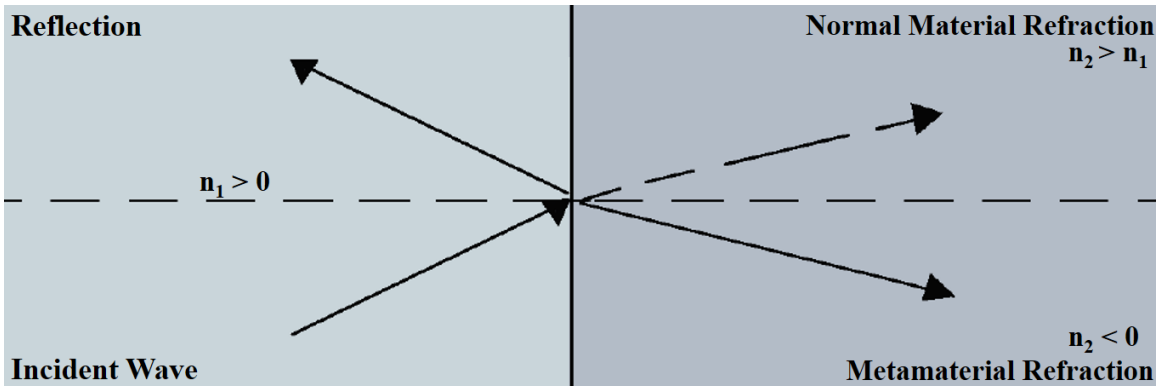

Figure 4. How a Wave Bends Based on Permittivity and Permeability. Adapted from [19].

The effective ε and μ of a MM can be defined as two complex values that are dependent on the applied frequency; Equations 4 and 5 [20].

$$\tilde{\varepsilon}(\omega) = \varepsilon_1 + i\varepsilon_2 \tag{4}$$

$$\tilde{\mu}(\omega) = \mu_1 + i\mu_2 \tag{5}$$

Typically, the real components, ε_1 and μ_1, are the focus in research for negative index of refraction by minimizing the losses of the imaginary components, ε_2 and μ_2 [21]. Metamaterial absorbers (MMA), however, optimize the structure and utilize the imaginary component to create a high absorption, as demonstrated in [17], [20] and [21]. Examples of MMA unit cells are in Figure 5 (a). MM perfect absorbers are generally designed to have 3 layers, a resonator, a metallic layer and a dielectric spacer in-between [22]; Figure 5 (c).

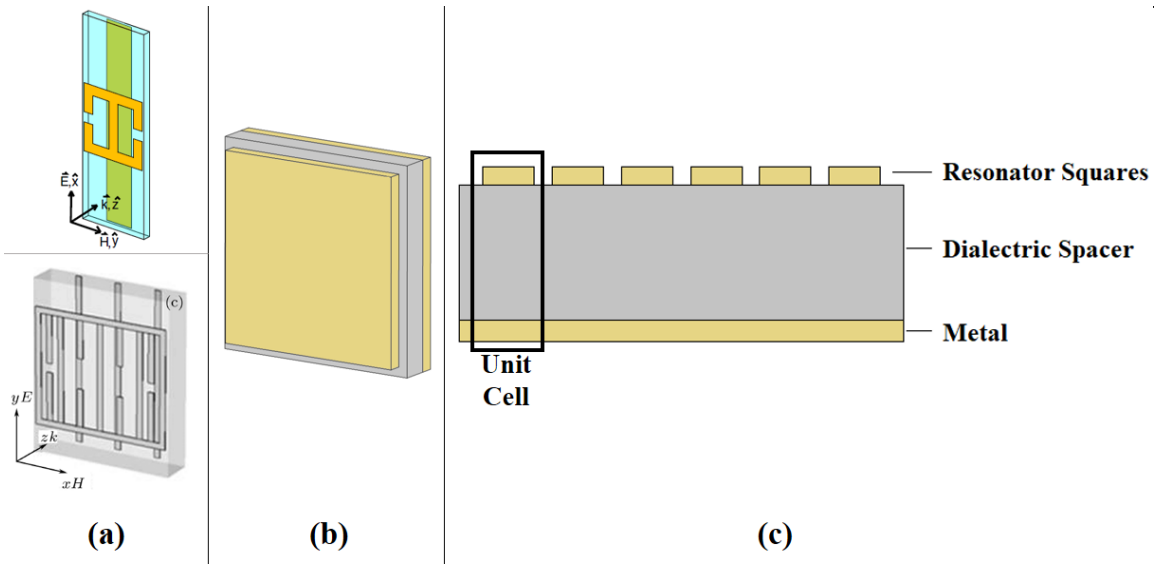

Figure 5. (a) MMA Unit Cell Examples. Sources: [20], [23]. (b) Generic MMA Unit Cell. Adapted from [5], [6]. (c) Generic Cross-Sectional Area MMA Sketch.

The losses that occurs in a MMA are a result of electrons oscillating in the plane where the dielectric and resonator metal meet, also known as plasmonic physics [24]. When the incident wave of resonant frequency is applied to the MMA, the electrons in the plane will oscillate, which results in the energy dissipating into the dielectric material through joule heating [24]. By adjusting the thickness of the dielectric material and resonator square size, the MMA can be optimized to absorb a specific frequency [22]. The absorption that occurs in the dielectric material is within a narrow frequency range. Wide-Band absorbers, however, have been demonstrated through the stacking of multiple unit cells [6].

C. ENHANCEMENT NMOSFET OVERVIEW

A FET is a type of semiconductor where the flow of current between its terminals can be regulated. Each FET has three terminals, a gate, a drain and a source as seen in Figure 6. By varying the electric potential applied to the gate, the current flowing between the drain and source can be controlled. The gate itself does not have any current flowing into its terminal when a voltage is applied. For this thesis, enhancement n-type Metal Oxide Semiconductor FET (NMOSFET) was used on the MM board. A

NMOSFET is a type of FET that is easy to fabricate, has a small geometry and low power dissipation, making it ideal for integrated circuits [25].

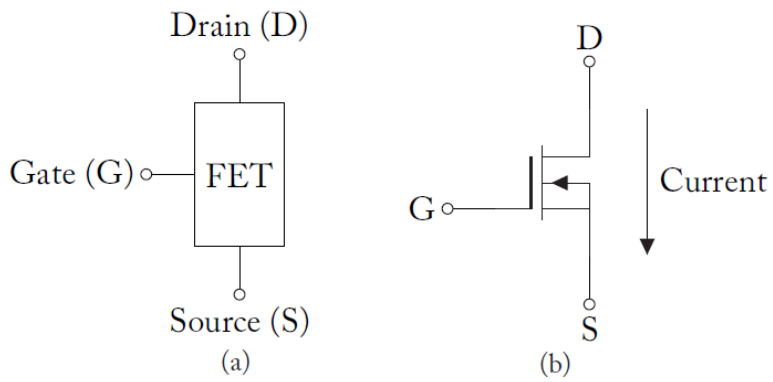

Figure 6. (a) Block Diagram of an FET. (b) NMOSFET Circuit Drawing. Adapted from [25].

N-type and P-type doped materials are used to create a NMOSFET. To dope a substance, a pure semiconductor, like silicon, has a different material added to increase the number of electrons or holes (positive carriers) in the substance. A N-type doped material has more electrons, creating more negative charges compared to the pure semiconductor used. A P-type doped material has more holes, creating more positive charges compared to the pure semiconductor. The source and drain of the NMOSFET are N-type materials while the bulk material is a P-type material. The gate is connected to a metal plate that is electrically separated by an oxide layer in the NMOSFET. Figure 7 is a sketch of the NMOSFET. The depletion zone is a region where there is no charge because of the interaction between the N-type and P-type materials.

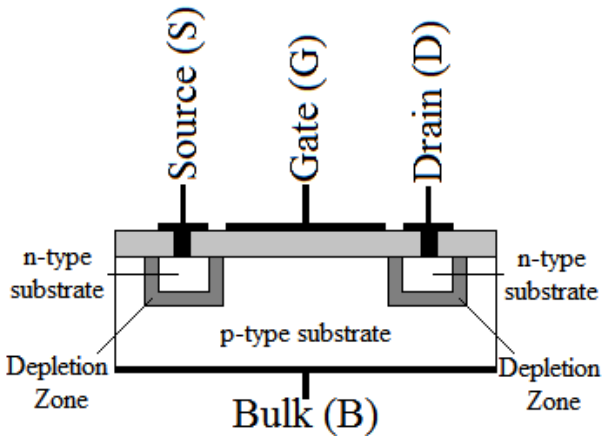

Figure 7. NMOSFET Design Sketch. Adapted from [25].

Each NMOSFET has a threshold voltage (V_{th}) based on the design characteristics and material of the NMOSFET. When the difference between the gate and source voltage (V_{gs}) is below the V_{th}, the positive charges in the P-type material are pushed away, creating a depletion zone between the two N-type materials. This prevents current to flow in the NMOSFET [25]. Once V_{gs} is above V_{th}, electrons in the P-type material are attracted to the gate, creating a channel between the two N-type materials. The channel created allows current to flow between the drain and source terminals. The current flow between the source and drain is dependent on the difference between drain and source voltage (V_{ds}) and the region of operation the FET is operating in. Figure 8 shows the current and voltage (I-V) curve for the drain current and V_{ds} as well as the regions of operation for the FET. The Δ represents a voltage difference being added to V_{gs}.

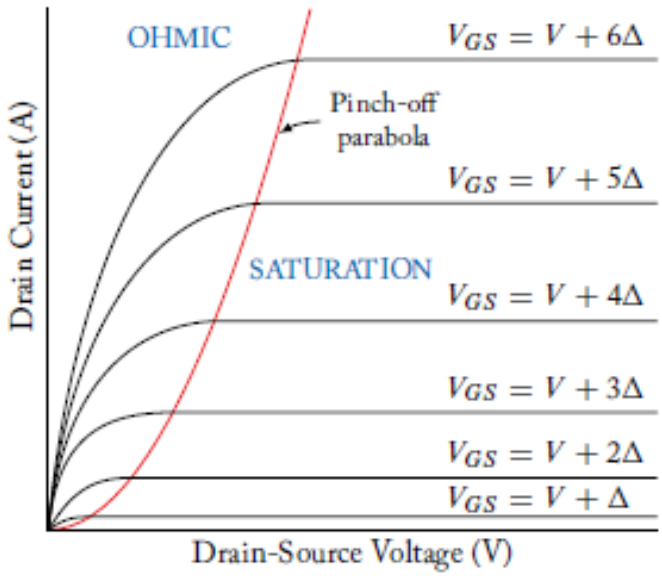

Figure 8. NMOSFET Regions of Operation. Source: [26].

The two regions of operation for enhancement NMOSFET, as well as all FET's, are the ohmic and saturation region. In the ohmic region for an enhancement NMOSFET, V_{gs} is above the V_{th}, V_{ds} increases based on Equation 6, where the variable *k* is a constant based on the FET characteristics [26].

$$I_d = k[2(V_{gs} - V_{th})V_{ds} - V_{ds}^{\ 2}] \tag{6}$$

The pinch off parabola is the V_{ds} point in which the enhancement NMOSFET switches from the ohmic region to the saturation region and can be obtained by Equation 7 [26].

$$I_d = kV_{ds}^{\ 2} \tag{7}$$

Once in the saturation region, the current for the enhancement NMOSFET is regulated at a constant current, as seen in Equation 8 [26].

$$I_d = k(V_{gs} - V_t)^2 \tag{8}$$

The higher the V_{gs}, the larger the slope in the ohmic region and the higher the maximum current is in the saturation region.

THIS PAGE INTENTIONALLY LEFT BLANK

III. METAMATERIAL BOARD DESIGN

The MM board was designed to be a single-band frequency absorber in the microwave domain. The board was designed at NPS and fabricated at a printed circuit board (PCB) manufacturer, PCB Universe. This fabrication method allows for the development of cost-effective boards with quick turnaround for initial testing. This method, however, doesn't allow for the control of the thickness of each layer. Seven millimeter (mm) resonator squares were chosen for the board, which achieves the peak absorption at an approximate resonant frequency of 9.1 GHz (wavelength of 3.3 centimeters [cm]). The length of the seven mm resonator square is approximately 4.7 times smaller than the resonant wavelength. The expected resonant frequency was approximated by examining the inverse relationship of the resonator square with the corresponding resonant frequency [17]. Figure 9 shows previously collected data for the eight, nine and ten mm single band absorbers [5], a linear fit can be used to approximate the resonant frequency.

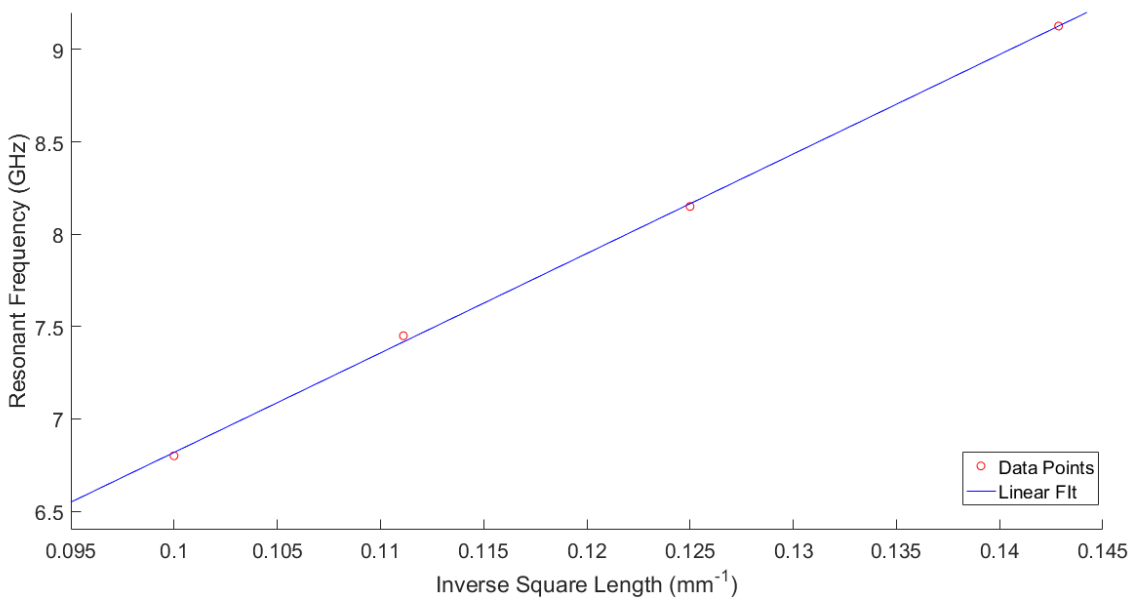

Figure 9. Resonant Frequency vs. Inverse Resonant Square Length. Adapted from [5].

The mm board, Figure 10 (a), is a 21 cm by 21 cm square board with three layers: a ground plane layer, a dielectric spacer layer and a resonator layer. The ground plane layer is a sheet of copper with a thickness of 55.1 micrometers (µm). The dielectric layer is composed of FR4 (standard PCB material) with a thickness of 836.7 µm. The surface layer consists of 20 x 20 seven mm squares spaced out by a constant gap of three mm between each square. Each square is composed of copper with a thickness of 38.2 µm. All thickness measurements were made with a scanning electron microscope. Figure 10 (b) shows a unit cell of a MM board consists of a single square, the space from one square to another, and all the layers underneath.

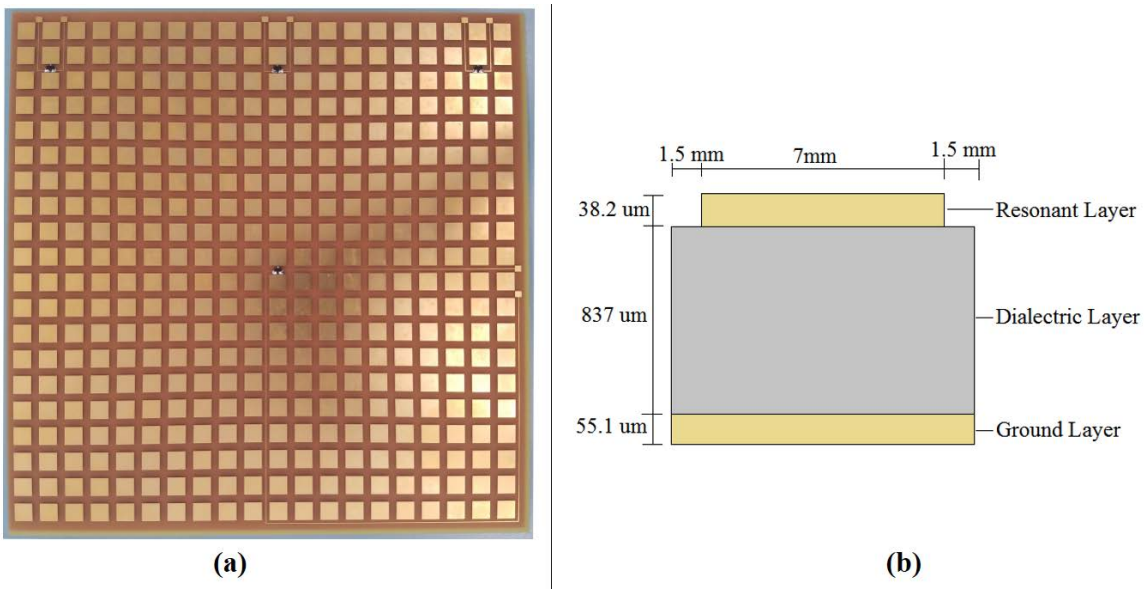

Figure 10. (a) Seven mm MM Board with FETs. (b) Sketch of the Cross-Sectional Area a Unit Cell.

Four FETs are placed on the board, with one in the center and three on one side of the board. The FETs are placed in the three mm square separation space. The gate and source of each FET have probing points on the board. The drain of the FET has a copper probe inserted into the MM board unit cell dielectric layer, Figure 11 (a). The probe connects to the FET by a via and a soldering test pad. The probe is 69.7 µm above the ground plane, a length of 1.4 mm, width of 1.8 mm and is 74 µm thick. Figure 11 (b)

shows a sketch of the FET circuit, with the drain in the unit cell, created on the MM board. Figure 11 (c) shows how the probe is connected to the FET.

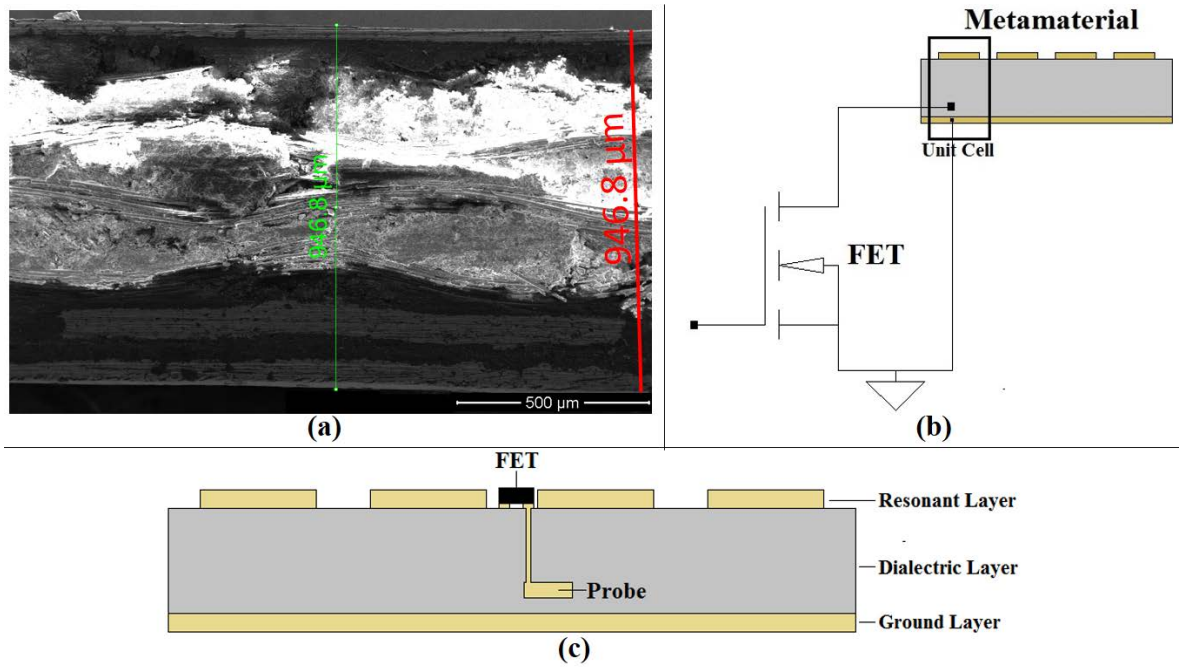

Figure 11. (a) SEM Micrograph of the Cross-Sectional Area with FET Probe. (b) FET Circuit Sketch with MM. (c) 2-D Sketch of MM Board Cross Section with FETs.

The expectation of the MM board is to generate a measurable electric potential between the probe and ground plane when absorbing the resonant frequency. The electric potential is applied to the drain of the FET, which is biased at the gate, to generate a current. When not at resonant frequency, current should be negligible or will flow at a reduced rate.

THIS PAGE INTENTIONALLY LEFT BLANK

IV. EXPERIMENTAL SETUP

A. MODELING

Simulation of the MM board is conducted with a finite element model. The COMSOL Multiphysics program with the Radio Frequency (RF) physics module was utilized for the simulations. The models utilized are based on McMahan's thesis that measured single band absorption for eight, nine, and ten mm boards [5].

Two COMSOL models were utilized for simulations, a seven mm resonator square model and a seven mm resonator square model with a probe inserted into the dielectric material. Figure 12 (a) and (b) are 2-D sketches of the unit cell models. The models are made with the parameters outlined in Chapter III. The FR4 in the model had the permittivity set to 4.3 and the tangent loss set to .0026 [5]. The model with the probe, Figure 12 (b) does not include the via and test pad used to connect the probe to the FET. The use of two models allowed for a direct comparison on how the probe may affect peak resonant frequency and absorption percentage. Both models, however, represent a MM board with a periodic structure with all the unit cells either having or not having probe points in the dielectric. The actual MM board fabricated consists of unit cells without a probe along with four-unit cells with a probe in the dielectric, so any effect estimated using the model will be smaller in reality.

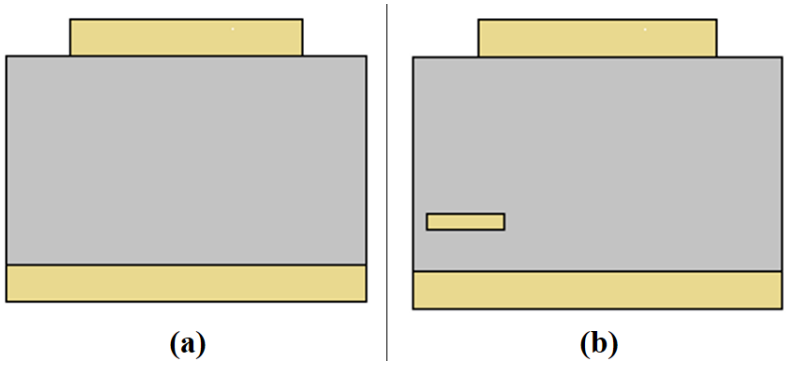

Figure 12. (a) 2-D Sketch of Seven mm COMSOL Model. (b) 2-D Sketch of Seven mm Unit COMSOL Model with Probe Inserted.

Two ports were used to calculate the scattering parameters of the unit cell surface and as a receiver for signals transmitted through the unit cell. The E&M wave radiated by the transmission port, travels perpendicular to the surface of the unit cell. Figure 13 shows a 2-D sketch of the port positions and boundary conditions, discussed later.

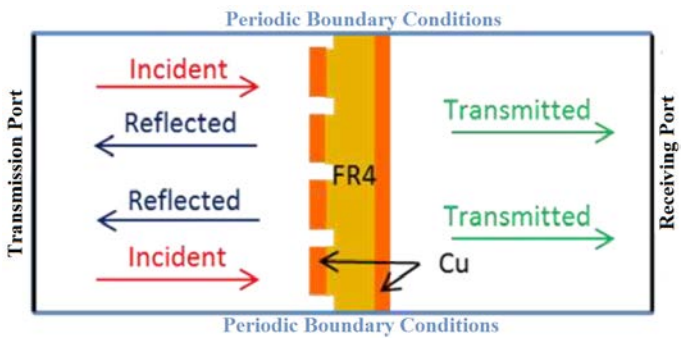

Figure 13. 2-D Port and Boundary Diagram. Adapted from [5].

To represent the actual power used by the port in the model, the antenna power is calculated as the power of a point source radiating isotopically over the antenna solid angle and multiplied by the specific antenna gain. The total output power of the source is represented by Equation 9

$$p_o = p_{in} E_{ant}\,, \tag{9}$$

where p_{in} is the power entering the antenna and E_{ant} is the efficiency of the antenna to utilize the power. Assuming the antenna has an efficiency of 100% ($p_o = p_{in}$), the power applied to a unit cell located at R distance from the antenna is given by Equation 10:

$$p_{sq} = \frac{p_{in}}{4\pi}\frac{A_{res}}{R^2}10^{G_{dBi}/10}\,, \tag{10}$$

where $\frac{p_{in}}{4\pi R^2}$ is the power density at R assuming the source radiates isotopically, A_{res} is the area of the resonator square and G_{dBi} is the logarithmic gain of the antenna compared to an isotopic source. Using a gain for the antenna of 11 dBi, the total length of the antenna being 98.52 mm distance, an input power of 20 mW and an area of 49 mm^2 in

Equation 10, the output power onto the unit cell resonator, and used in the model, was 101.1 μW. In other words, the maximum achievable power, when the antenna is placed directly on top of the MM, was 101.1 μW

The boundary conditions of the model space need to be set properly to represent the periodic structure of the MM board. With the port sending waves perpendicular to the structure (normal incidence), perfect electrical conductor (PEC) boundaries are set in the yz-planes and perfect magnetic conductor (PMC) boundaries in the xz-planes, perpendicular to the electric fields and magnetic fields generated, respectively. The PEC and PMC boundaries enforce the periodic boundary conditions for the electric and magnetic fields normal to their respective boundaries (Only true for normal incidence) [27], as seen in Figure 13.

Once the boundaries, ports and meshing are set, a simulation is conducted that that solves for the effects of the E&M waves on the unit cell at varying frequencies. The simulation is performed in the frequency domain and does a frequency sweep from 5 to 15 GHz. Once the COMSOL study is complete, the absorption is calculated with a volumetric integration of the resistive losses of the unit cell [5]. The results can be divided by the input power and multiplied by 100 for the percentage of power absorbed in the MM board. These calculations are done with the assumption that magnetic losses are negligible [5].

To simulate the electric potential between the probe and ground plane, a lumped port is inserted into the model [28]. The lumped port is added by creating a 2-D plane that is centered on the probe. For the lumped port to operate properly, a perfect electrical conductor (PEC) is placed on each end of the lump port, which is consistent with the fact that they are placed within the metal volume in the model. One PEC is placed inside the probe and the other is placed in the ground plane, as seen in Figure 14.

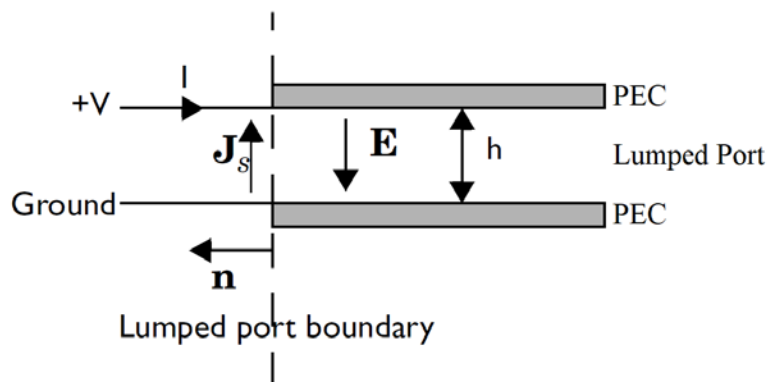

Figure 14. Lumped Port Diagram. Adapted from [28].

COMSOL performs a mathematical calculation based on the results of the simulation to estimate the electric potential created from the electric field generated in the lumped port; Equation 11 [28].

$$V = \int_h E \cdot dl = \int_h (E \cdot a_h) dl \tag{11}$$

V is the electric potential, E is the electric potential, h is the length of the lumped port between the PECs and a_h is the direction of electric field between lumped port. The results from the calculation provides the peak voltage, V_p, for the AC voltage created for each simulated frequency.

Conducting simulations for the absorption of the unit cell and for the electric potential must be performed as separate simulations. The lumped port for the electric potential analysis must be removed from the probe model to get accurate absorption data. The lumped port calculations turn out to affect the volume integration for resistive losses conducted on the unit cell.

Using the electric potential found from the COMSOL model, a spice simulation model, shown in Figure 15, is utilized to calculate potential IV curves of the FET. The source of the FET is grounded, with a voltage source attached to the gate and drain. The voltage at the gate represents the bias voltage applied to the FET that would have to be provided in the sensing MM. The spice simulation does a sweep of the drain voltage from

zero volts to the RMS voltage value, V_{rms}, at the resonant frequency, solved using Equation 12.

$$V_{rms} = \frac{V_p}{\sqrt{2}} \tag{12}$$

The spice model simulates the IV characteristics of the FET based on the frequency applied to the MM board. The max voltage value of the sweep correlates to the resonant frequency of the MM board, as it will be shown in the next chapter.

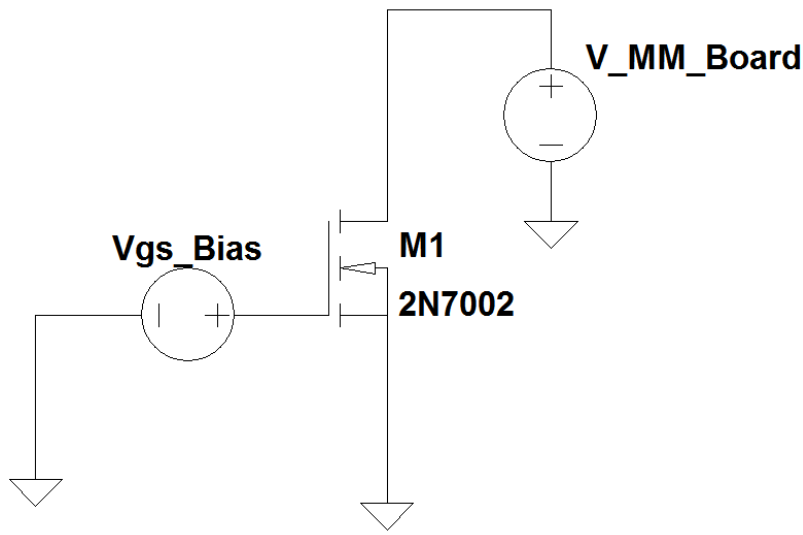

Figure 15. SPICE Simulation Model.

B. CHARACTERIZATION SETUP

Absorption data was collected with the same method utilized for the single band absorbers reported in [5]. Figure 16 shows a block diagram and a picture of the experimental apparatus used to make the absorption measurements of the MM board. The sweep oscillator created the E&M waves that were sent to the transmission horn antenna. The horn antenna then transmitted the waves onto the MM, which created reflected waves that were received by the receiving horn antenna. The spectrum analyzer measured the power of the waves received in a series of discrete points. Anechoic tiles were placed

at the base of the experimental apparatus to reduce potential reflections could occur from the tiled floor.

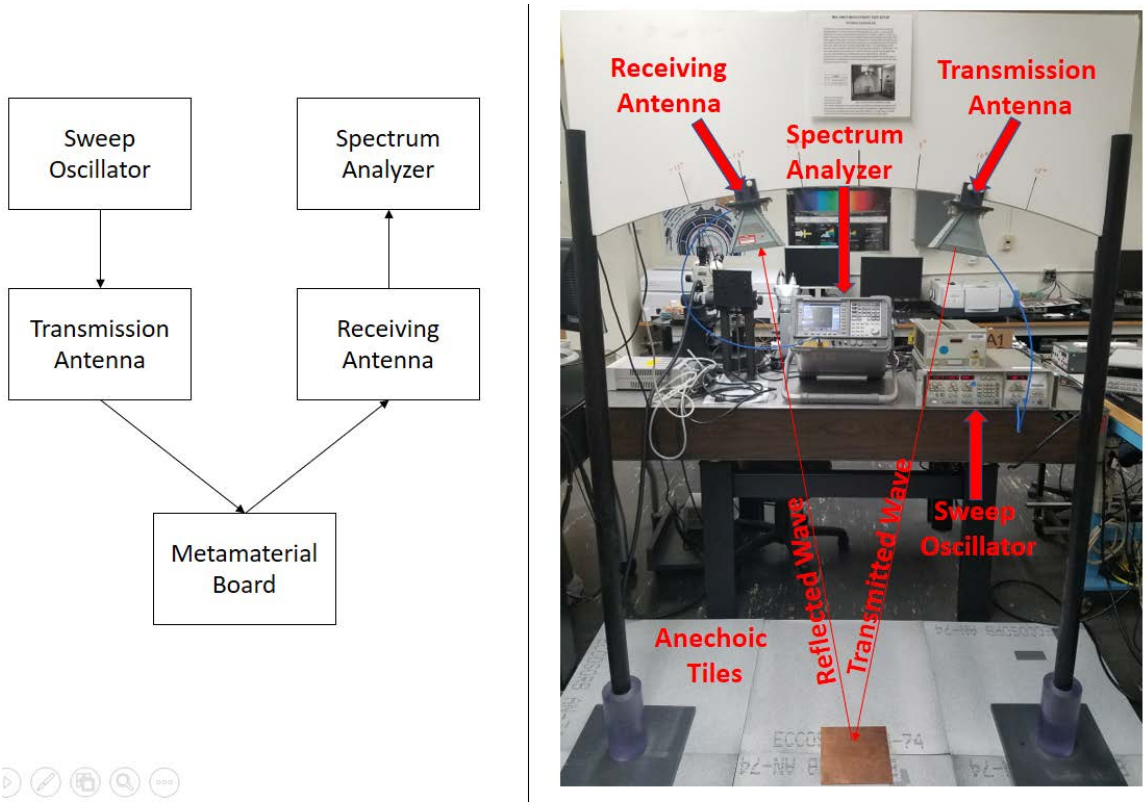

Figure 16. Absorption Apparatus Block Diagram and Experimental Setup.

For each experimental run, the sweep oscillator performed a sweep of E&M waves from frequencies of 5 GHz to 15 GHz. The horn antennas were placed 5 degrees' off the normal of the MM board for the measurements. The spectrum analyzer was set-up to collect 1000 points of data within the same frequency range as the sweep oscillator. Two sets of measurements were taken: one with a mirror plane and one with the MM board. The mirror plane is a solid copper surface that has the same area as the MM board, which is assumed to have 100% reflection for the frequency band of interest. The absorption of the MM board is calculated by utilizing both sets of data in Equation 13 [5].

$$A = 100 * (1 - \frac{P_{metamaterial}}{P_{mirror}}), \tag{13}$$

where A is the absorption of the MM, $P_{metamaterial}$ is the reflected power of the MM and P_{mirror} is the reflected power of the mirror plane.

C. SENSING CHARACTERIZATION SETUP

Once the resonant frequency was identified, wires were soldered onto a MM board to analyze the FET when the E&M field is applied; Figure 17 (a). The wires were attached to a semiconductor device analyzer to analyze the I-V curves created in the FET at when E&M waves were applied to the MM.

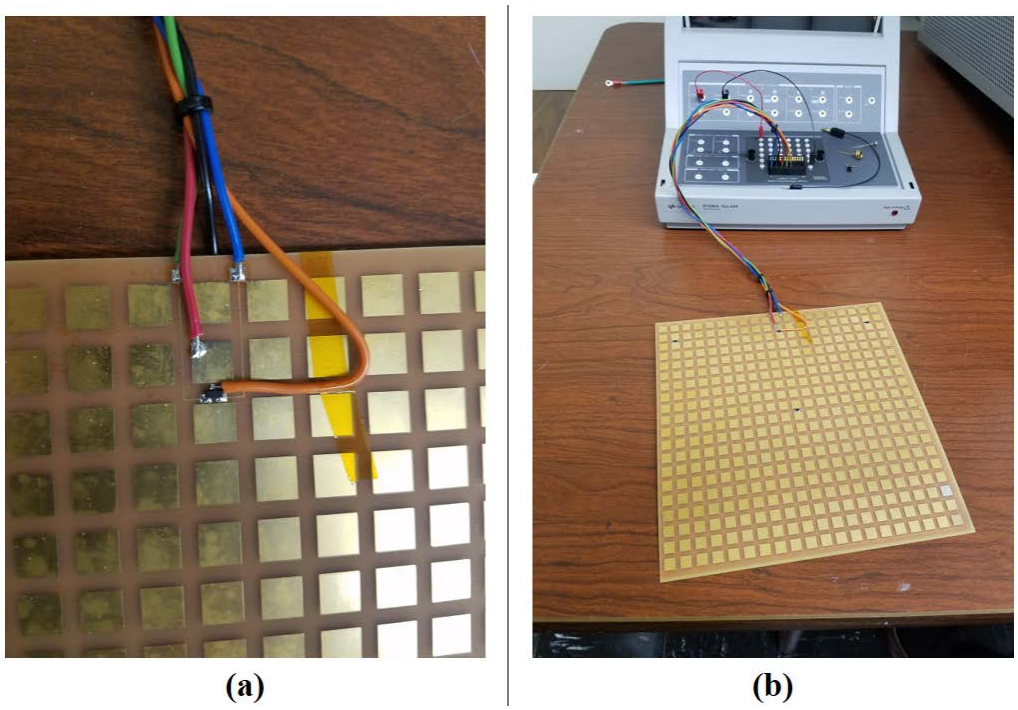

Figure 17. (a) Wire Soldering onto MM Board. (b) MM Board Hooked up to Device Analyzer.

To analyze the effects of applying a E&M field on the MM board, the sweep oscillator generated a continuous signal at a frequency previously determined to be resonant with the transmitting horn antenna placed as close to the MM board as possible. I-V curves of the FET were created by the semiconductor device analyzer for an analysis of applying E&M fields at different frequencies onto the MM board. To see if the E&M

wave had any effect, changes in the I-V curves were analyzed to identify any differences in the curves. With the current configuration of the MM board, when the resonant frequency E&M wave is resonating, a current would flow through the FET, creating a change in the I-V curve compared to no E&M wave radiating, indicating that an electric potential is generated.

V. RESULTS

A. ABSORPTION RESULTS

The experimental reflection data collected for the mirror plate and the MM board was processed through a moving average filter, the smooth() function in MATLAB. Figure 18 shows both the raw data and the filtered data of the reflections. Below 8.5 GHz and above 10 GHz the reflected signals show similar patterns of reflections except for the amount of power reflected. The difference in the absolute value of the power can be a result in slightly different positioning of the MM board and the mirror plane or the difference in the curvature of the board, discussed more in appendix B. Between 8.5 GHz and 10 GHz is where the reflections do not match. The MM Board has a lower power compared to the mirror plane. This is the region where the absorption in the MM board has occurred. The large spike that occurs between 6.3 and 6.7 GHz is a result of an impedance jump in the spectrum oscillator, but is removed by Equation 13 and not present in Figure 19.

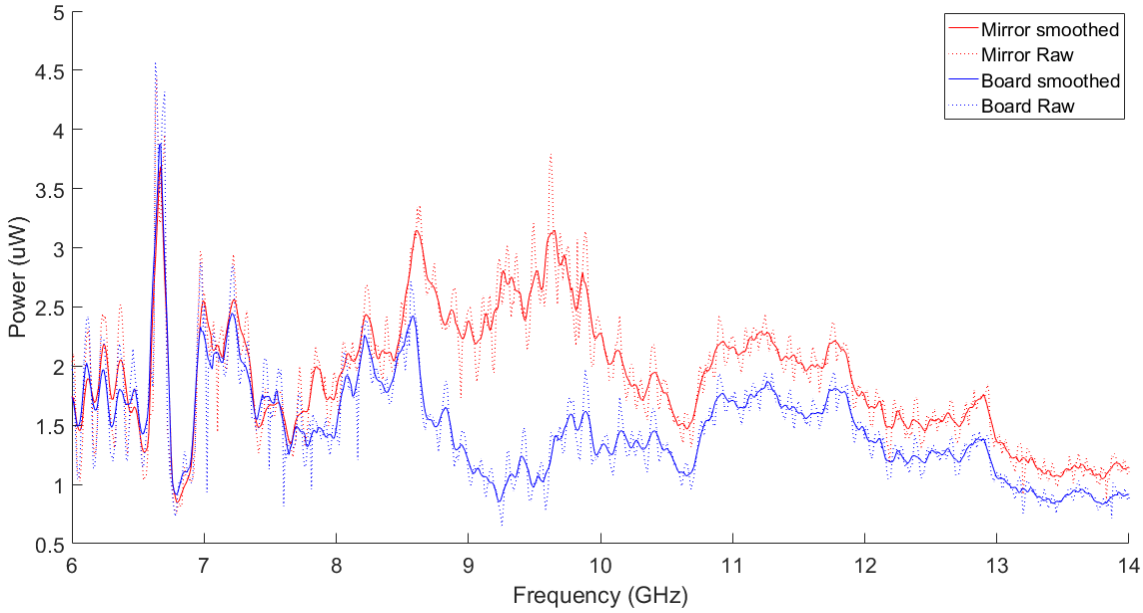

Figure 18. Mirror and MM Board Reflection Data.

The smoothed reflected data for the mirror and MM board were used in Equation 13 to find the narrowband frequency range absorption for the MM board. The experimental absorption results for the MM board as well as two theoretical absorption results are found in Figure 19.

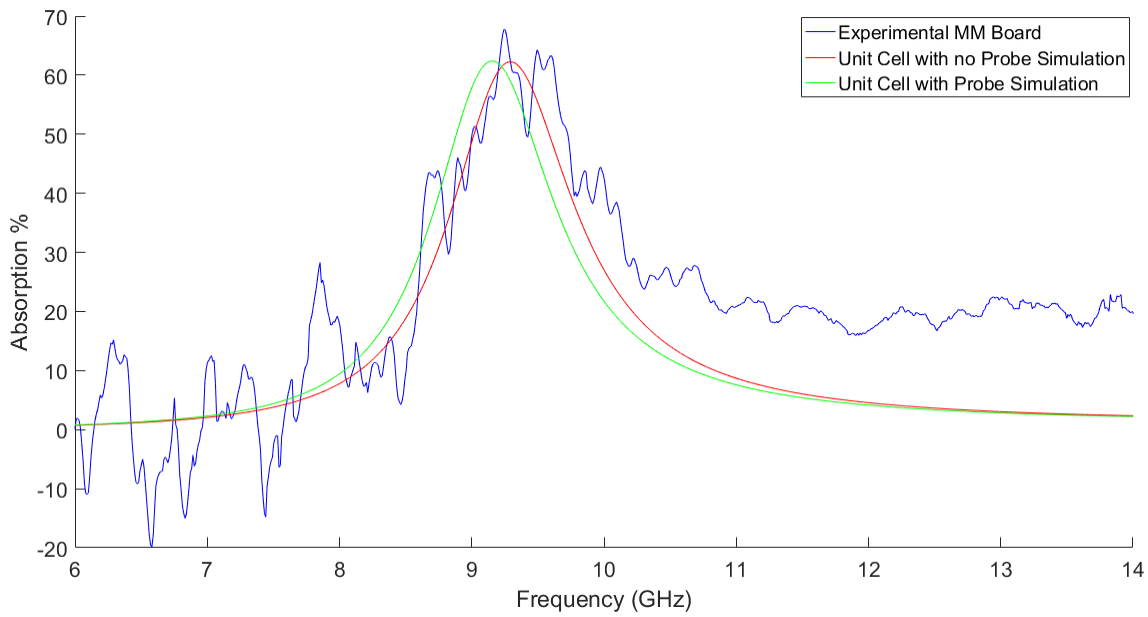

Figure 19. MM Board Simulation and Experimental Absorption.

The peak absorption for the experimental data occurs between 9.25 GHz and 9.6 GHz, which is in good agreement with the prediction made in Chapter III. The absorption, based on the three peak values within the peak frequency range, averaged to 65%. After 10.3 GHz, the absorption, on average, does not return to 0% but stays, on average, at about 20%. For the seven mm board with no probe simulation, the absorption peak occurs at 9.3 GHz with a 62% absorption. For the seven mm board with the probe simulation, the absorption peak occurs at 9.15 GHz with an identical absorption. The theoretical absorption plot without a probe correlates better with the experimental results collected. This was expected since most of the unit cells on the MM board do not contain probes. When a probe is inserted into all the unit cells, the resonant frequency shifts to the left 130 Megahertz.

Figure 20 shows a comparison of the absorption data for MM boards with eight and nine mm resonator squares from the previous work and the current experimental MM board. All experimental reflection data was processed through the MATLAB smooth() function before solving for the absorption and being plotted.

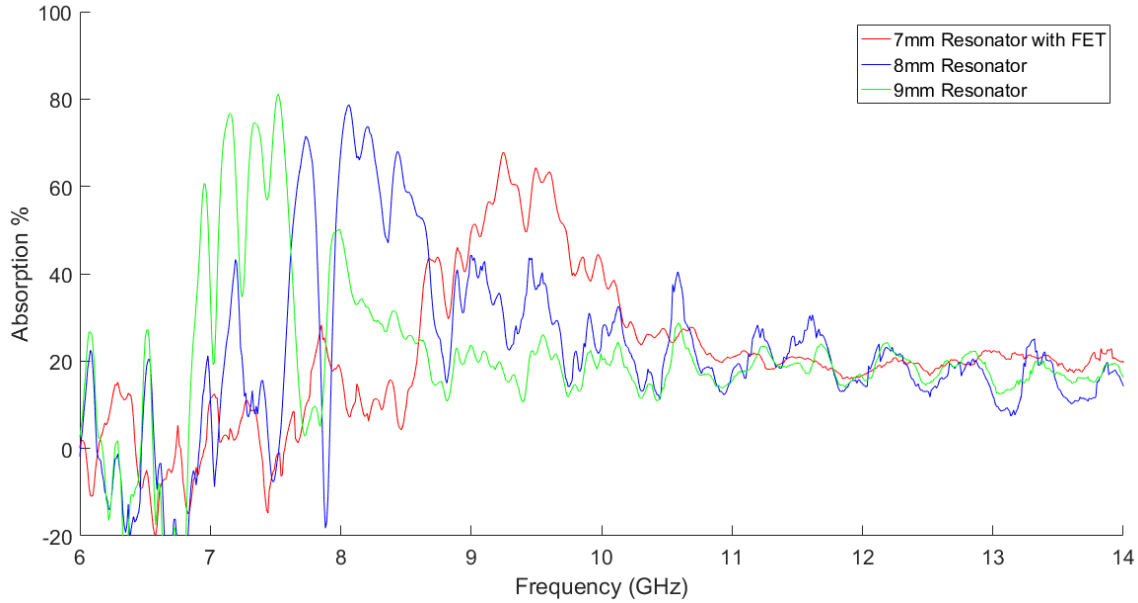

Figure 20. Experimental Absorption with Different Resonator Square Sizes.

As the resonator squares get smaller, the resonant frequency shifts to the right. The absorption data for the eight and nine mm resonator MM boards also settle at 20% absorption after the expected absorption curve. This absorption of 20% may be a result of the slight difference in position of the mirror plane and MM board, the difference in bend of the MM board and mirror plane or the experimental apparatus itself.

B. SENSING RESULTS

For the model with the probe, the simulated electric potential created in the lumped port contained a real and imaginary component. The magnitude of the electric potential and the electric potential's phase can be found knowing with the simulation data, as seen in Figure 21. The peak electric potential for the simulation occurs at 9.1 GHz and a 180 degree phase shift occurred at nine GHz. The peak voltage created in the

simulation occurred was 10.6 mV when a simulated power onto the square of 101 µW is applied to the unit cell.

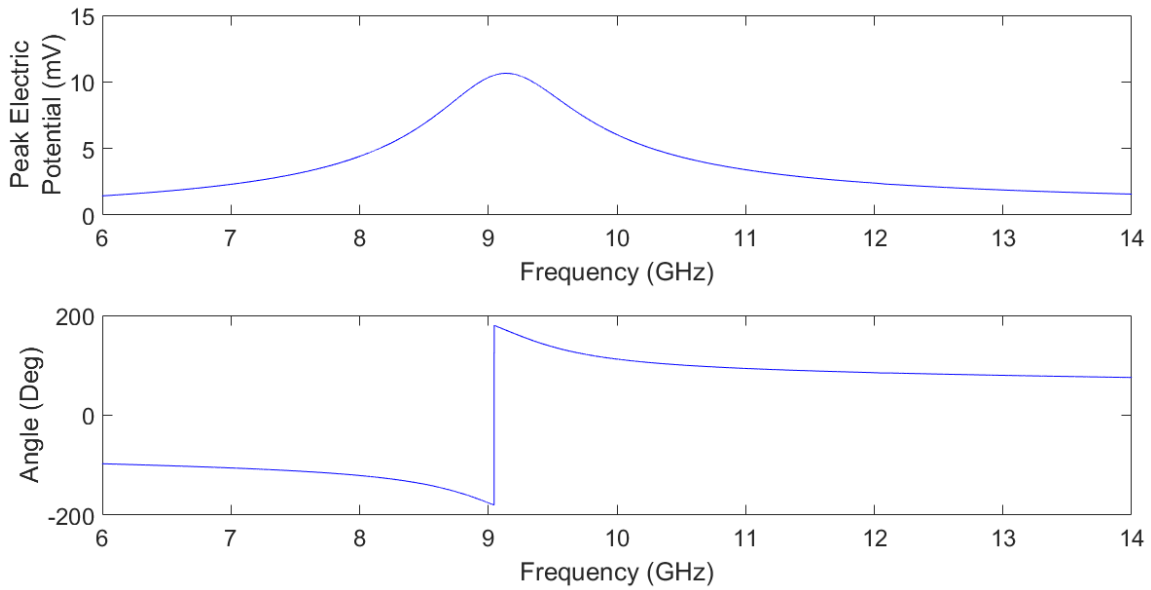

Figure 21. Simulation Electric Potential Magnitude and Phase.

Both the absorption and electric potential magnitude simulation data for the unit cell with a probe inserted are normalized and are shown in Figure 22. The peak values for both simulations are within 36 megahertz (MHz). of each other. Based on this, the peak electric potential will occur at the peak resonant frequency for absorption. The voltage graph is wider than the absorption graph, providing voltage values for frequencies that are partially absorbed in the narrowband frequency range.

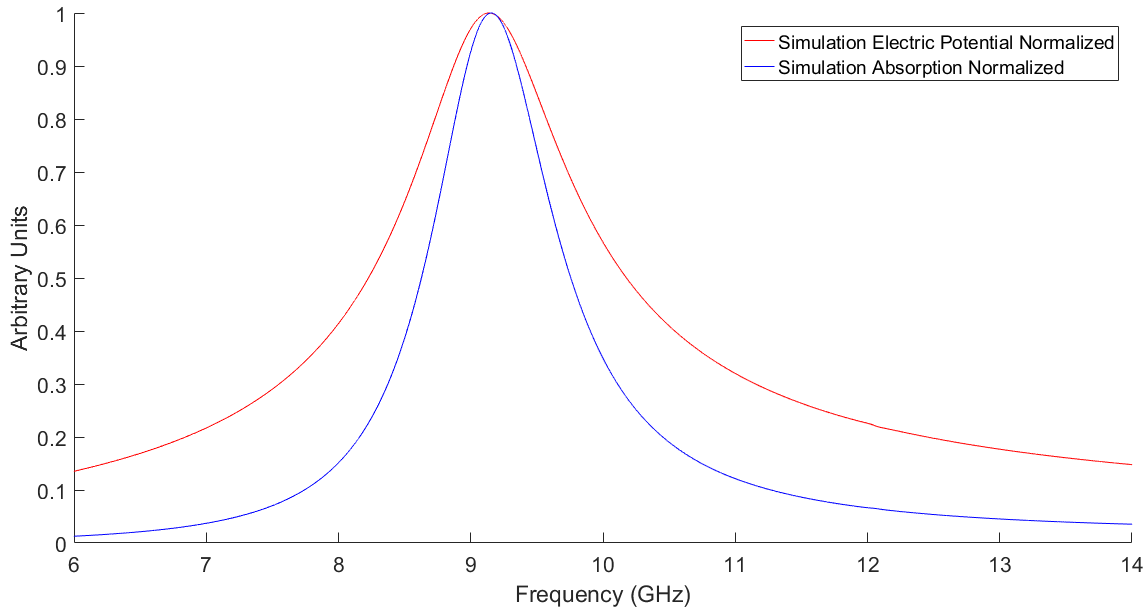

Figure 22. Normalized Absorption and Electric Potential from COMSOL Simulations

Figure 23 is the spice simulation results from a V_{ds} of zero volts, representing the sweep oscillator is off, to V_{rms} value of the peak voltage, representing the resonant frequency E&M being radiated onto the MM board. The results of the simulation show that the FET will operate in the Ohmic Region of the FET.

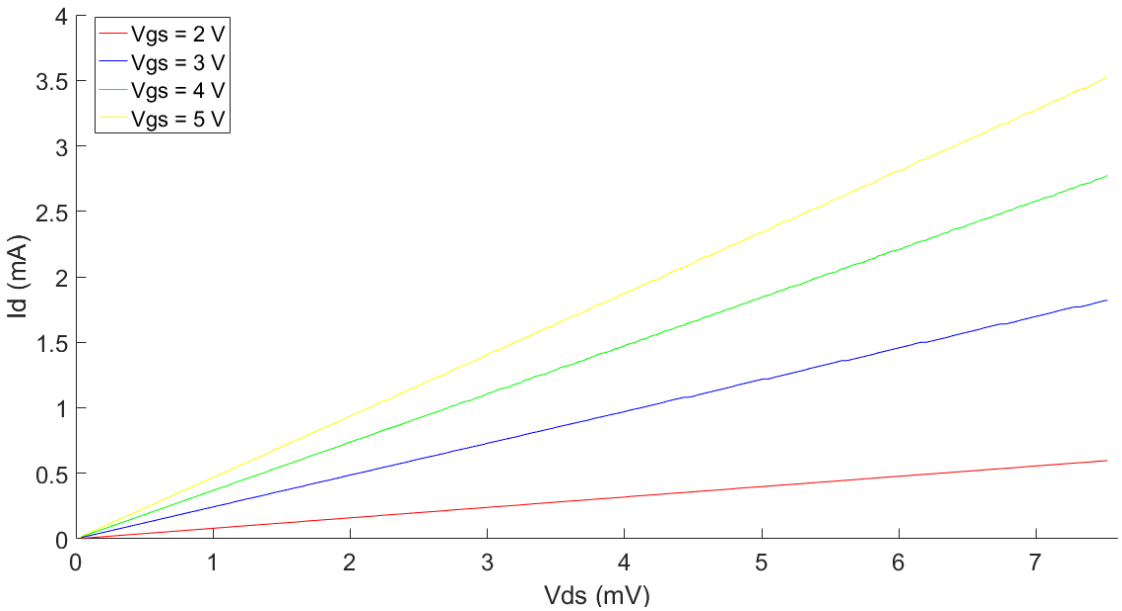

Figure 23. Spice Simulation FET Model.

No experimental data for the sensing characterization of the MM board was collected. When taking measurements with the semiconductor device analyzer, no difference in FET characteristics was noticeably visible with the sweep oscillator radiating and not radiating. A voltmeter was utilized to measure the electric potential. No difference in electric potential was identified between the probe and ground plane when radiating and not radiating. This may be a result of the high frequency signal or the limited electric potential generated.

C. PROBE POSITION ANALYSIS

An analysis was performed on the effect of the probe position on the absorption and electric potential measured in the simulation. The probe started at 59.6 um above the ground plane, and was move up in increments of 100 um up to 559.6 um. Figure 24 show the absorption at the varying heights respectively. The peak absorption percentage remains constant but the peak resonant frequency shifts to the left slightly, with 59.6 um probe height at 9.15 GHz resonant frequency and 559.6 um probe height at 9.0 GHz resonant frequency. A secondary absorption peak begins to appear as the probe gets

closer to the surface of the unit cell at 12 GHz. The secondary peak appears due to the probe acting as a secondary resonator as it approaches surface of the unit cell.

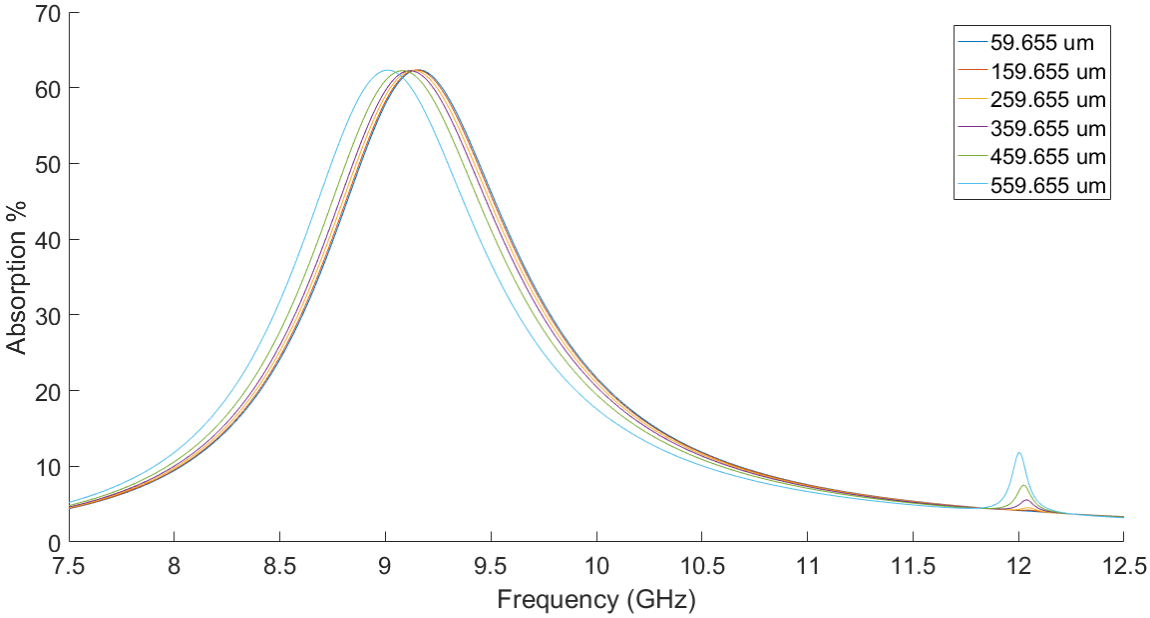

Figure 24. Simulated Absorption at Varying Probe Heights.

Figure 25 shows the magnitude and phase of the electric potential at different probe heights. As the probe gets farther away from the ground plane, the electric potential gets higher and the phase shift begins to appear at earlier frequencies. The peak electric potential at 559.6 um was 75 mV, with a difference of 63 mV between the original height. The frequency shift in both the absorption and electric potential may result from the resonator and probe in the dielectric getting closer together. This causes them to appear merged together, creating effective dimensions that make the resonator appear a different size.

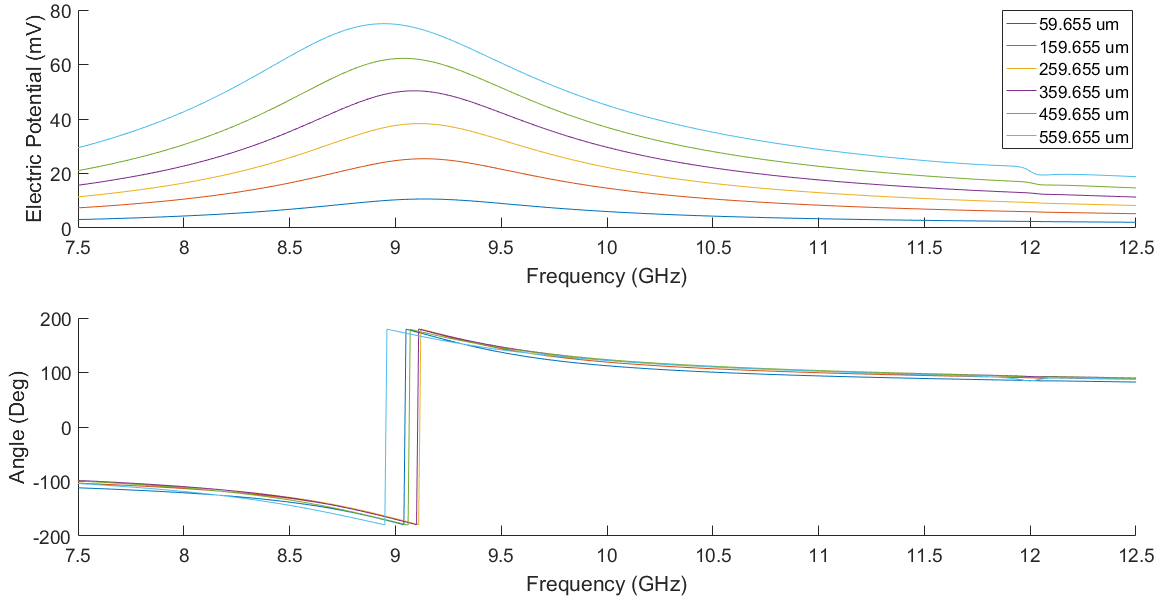

Figure 25. Simulated Electric Potential Magnitude and Phase at Varying Probe Heights.

VI. CONCLUSION

A. RESULTS SUMMARY

Experimental and simulated results for absorption characterization have shown the MM board design with the incorporated FET's continue to follow the expected behavior of the resonant frequency. The MM board experimental absorption correlated with the simulation with no probe. This is due to the number of probe unit cells being limited to just four, not impacting the overall absorption frequency peak. Simulations show for a MM board with all the probe unit cells, an expected shift to the left of the MM board resonant frequency. As the probe gets closer to the surface of the MM unit cell, simulations demonstrated the frequency will continue to shift slightly to the left with a smaller secondary absorption peak developing. The secondary peak is created due to the probe acting as a separate resonator plate.

Simulations demonstrated that an electric potential will be generated between the probe and ground plane that correlates to the resonant frequency of the MM board. The position of the probe determines the magnitude of the electric potential generated, with a larger electric potential generated as the distance between the probe and ground plane increases. Just like the absorption, the phase shift for the MM board will move to the left.

With simulated results of an RMS electric potential of seven mV applied to the drain, experimental results for sensing through the FET could not be collected. This could be a result of FET components or the test equipment not rated to measure the GHz range frequencies. The signal may also be smaller than the estimated simulated value and is getting buried in the noise generated from the equipment.

Overall, absorption characterization of the MM board could be performed experimentally and with simulations while the sensing characterization could only be demonstrated with simulations. The current MM board provided a limited amount of experimental tests that can be done due to having an FET integrated onto the circuit board. The next generation of MM boards for sensing should not contain any components integrated onto the board. Test points for the probe in the dielectric and the resonator

should be incorporated onto the MM board, as proposed in Figure 26. This will significantly broaden the number of experimental tests that can be done for the sensing characterization of the MM board.

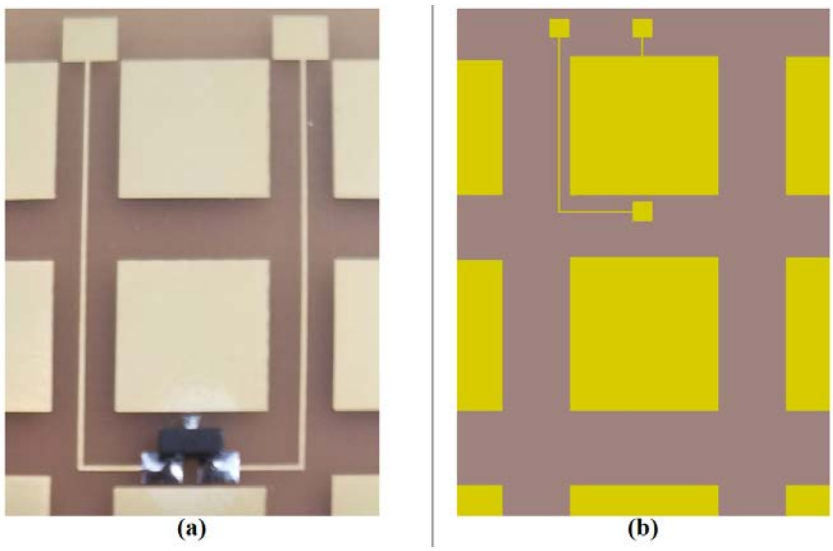

Figure 26. (a) Current MM Board Layout. (b) Proposed MM Board Layout.

B. FUTURE WORK

To continue working on MM sensing, an amplification of the electric potential from the probe is recommended. The increased AC voltage can be rectified to create a direct current (DC) voltage, as shown in Figure 27 (rectifier circuit). Using a DC voltage allows for multiple types of test equipment to be utilized for future MM sensing. Integration of the circuit simulation into COMSOL also needs to be conducted to develop more precise simulations.

1. Probe Voltage Amplification

The amplification of the probe electric potential can be conducted by amplifying the E&M field generated by the sweep oscillator. This is done by adding a signal amplifier between the sweep oscillator and transmission antenna. With a signal amplifier added, Equation 10 can be adjusted to incorporate the gain added by the signal amplified,

as seen in Equation 14. G_{dbi_Ant} is the logarithmic gain for the antenna and G_{dbi_SA} is the logarithmic gain of the signal amplifier.

$$p_{sq} = \frac{p_{in}}{4\pi}\frac{A_{res}}{r^2}10^{G_{dBi-Ant}/10}10^{G_{dBi_SA}/10} \tag{14}$$

A COMSOL simulation was used to find the incident power on the MM unit cell for the desired electric potential. The incident power on the unit cell can then be used to find the necessary input signal power at the horn antenna by using Equation 10. To get an electric potential with an approximate peak value of 200 mV, the transmission antenna would need to output eight watts of power. For a peak value of 100 mV, two watts of power would be required.

Another approach to amplify the probe output is to use a gain stage based on operational amplifiers (OPAMP). An OPAMP is placed before the rectifier circuit and amplifies the electric potential before it goes to the rectifier circuit, as shown in Figure 27 (OPAMP circuit). This addition to the circuit could provide the necessary additional gain required to get the desired electric potential.

Once the desired electric potential is achieved, a rectifier circuit can be implemented to turn the amplified AC value into a DC value. Figure 27 is an example of a potential block diagram using both a signal amplifier and OPAMP. Once the circuit is tested, future research can be conducted on integrating the circuit onto the MM board and implementing the circuit on flexible MMs.

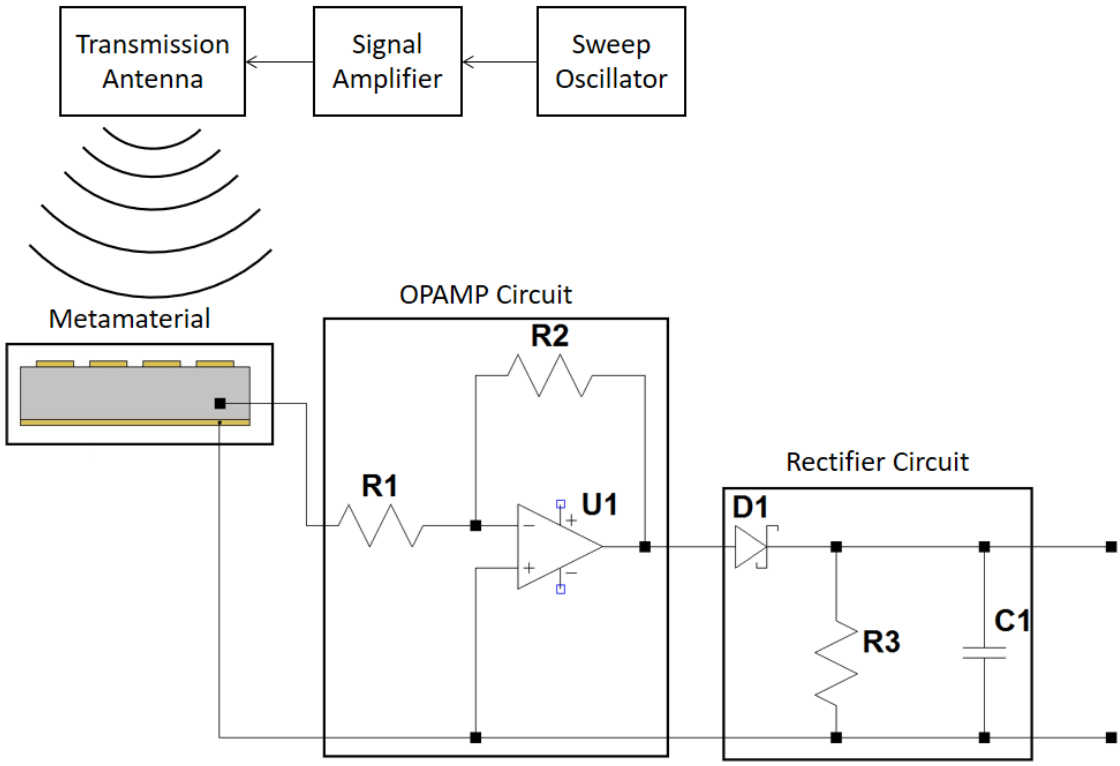

Figure 27. Example of Circuit for MM Board Sensing.

2. COMSOL Simulation Improvements

COMSOL Multiphysics program is a powerful program that breaks down physics simulations into different modules. A module not utilized in this thesis was the circuit module. Future research can be done in developing an integrated model utilizing the RF module and circuit module to show the interaction between the MM board and proposed circuit. This model would remove any ambiguity and approximations used when having a separate MM and circuit model.

Another improvement for future research is a more refined COMSOL model for the unit cell with the probe. The current model is missing the via and pad that is used to connect the probe to the FET. By introducing these design characteristics into the model, more accurate absorption and electric potential simulations can be conducted.

C. FINAL THOUGHTS

Through the research conducted in this thesis, the characterization of the MM board with FETs and simulation of the electric potential created in a MM at the resonant frequency was accomplished. By ability to experimentally measure the electric potential created at the resonant frequency, however, was not accomplished. Future work should continue to work toward the capability to experimentally measure the electric potential created as well as improve simulation models for more precise simulation results. By creating an electric potential and using circuitry to apply a DC voltage onto FETs, the capability to detect and characterize a HPM weapon threat becomes plausible based on the absorbed frequencies in the MM.

THIS PAGE INTENTIONALLY LEFT BLANK

APPENDIX A. MATLAB CODE

```
%This code provides examples of how in  and simulation data for the
%thesis was analyzed in MATLAB
%Clears the workspace, Command Window, and closes all Figures
clear; clc; close all
%Constant Values used in the script
sm_num = 10;                %Number of points used in smooth() function
Po = 101.52*10^-6;          %Used to calculate the absorption % for the
                            %simulations from COMSOL. Use the power from
                            %COMSOL
%Variables used for the filenames for ease of use later in the script.
%Experimental Data Files.
file = '20171019 8MMABS5DEG.CSV';
%Simultion Data Files
file = '20171102 No Gate Simulation Absorption.csv';
%7 MM Board Experimental Absorption Data Example
Exper_Freq = csvread(file,15,0,[15,0,1014,0]); %Frequency from file
Mirror_7mm = csvread(file,15,1,[15,1,1014,1]);    %Mirror Plane Data
Mirror_7mm_sm = smooth(Mirror_7mm,sm_num);  %Used to average the data
Board_7mm = csvread(file,15,2,[15,2,1014,2]);     %MM Board Data
Board_7mm_sm = smooth(Board_7mm,sm_num);    %Used to average the data
%Calculates the experimental absorption
Abs_7mm = (1-(Board_7mm./Mirror_7mm))*100;
Abs_7mm_sm = (1-(Board_7mm_sm./Mirror_7mm_sm))*100
%7mm Simulation Absorption Data Example
frequency_7mm_sim = csvread(file,5,0,[5,0,10004,0]);
Abs_7mm_sim = csvread(file,5,1,[5,1,10004,1])/Po;
%7mm Board Simulation Voltage Data Example
frequency_7mm_sim_wi_2 = csvread(file6,5,0,[5,0,10004,0]);
volt_7mm_sim = csvread(file6,5,1,[5,1,10004,1]);
magnitude = abs(volt_7mm_sim);
phase = angle(volt_7mm_sim)*180/pi;
%Example plot for Absorption Data.
figure (1)                      %Identifies the figure used
hold all                        %Allows for plotting multiple plots
set(gca,'fontsize',16);         %Sets font size
plot(frequency_7mm*10^-9,Abs_7mm_sm,'r')
xlabel('Frequency (GHz)')
ylabel('Absorption %')
%Example plot for electric potential data
figure (2)
hold all
subplot(2,1,1)                  %Subplot for magntitude
set(gca,'fontsize',18);
plot(frequency_7mm_sim_wi_2*10^-9,magnitude,'bl') %Magntiude plot
xlabel('Frequency (GHz)')
ylabel('Electric Potential (mV)')
subplot(2,1,2)                  %Subplot for phase
plot(frequency_7mm_sim_wi_2*10^-9,phase,'bl') %Phase plot
xlabel ('Frequency (GHz)')
ylabel('Angle (Deg)')
```

THIS PAGE INTENTIONALLY LEFT BLANK

APPENDIX B. METAMATERIAL CURVITURE

When conducting measurements to get absorption data on the MM board, it is important to check the curvatures of the mirror plane and the MM board. The mirror plane reflection measurements and MM board measurements need to have the same curvature for accurate results, with the preference being completely flat. This allows for the same reflection path for both the MM board and mirror plane. Even the slightest bend in the MM board or mirror plane can create different reflection paths, skewing or even invalidating any results collected. If the ground plane of the MM board is used as the mirror plane, a bend can result with a mirror plane that is concave and a MM board that is convex, creating two completely different paths of reflection

THIS PAGE INTENTIONALLY LEFT BLANK

APPENDIX C. ADDITIONAL COMSOL MODEL IMAGES

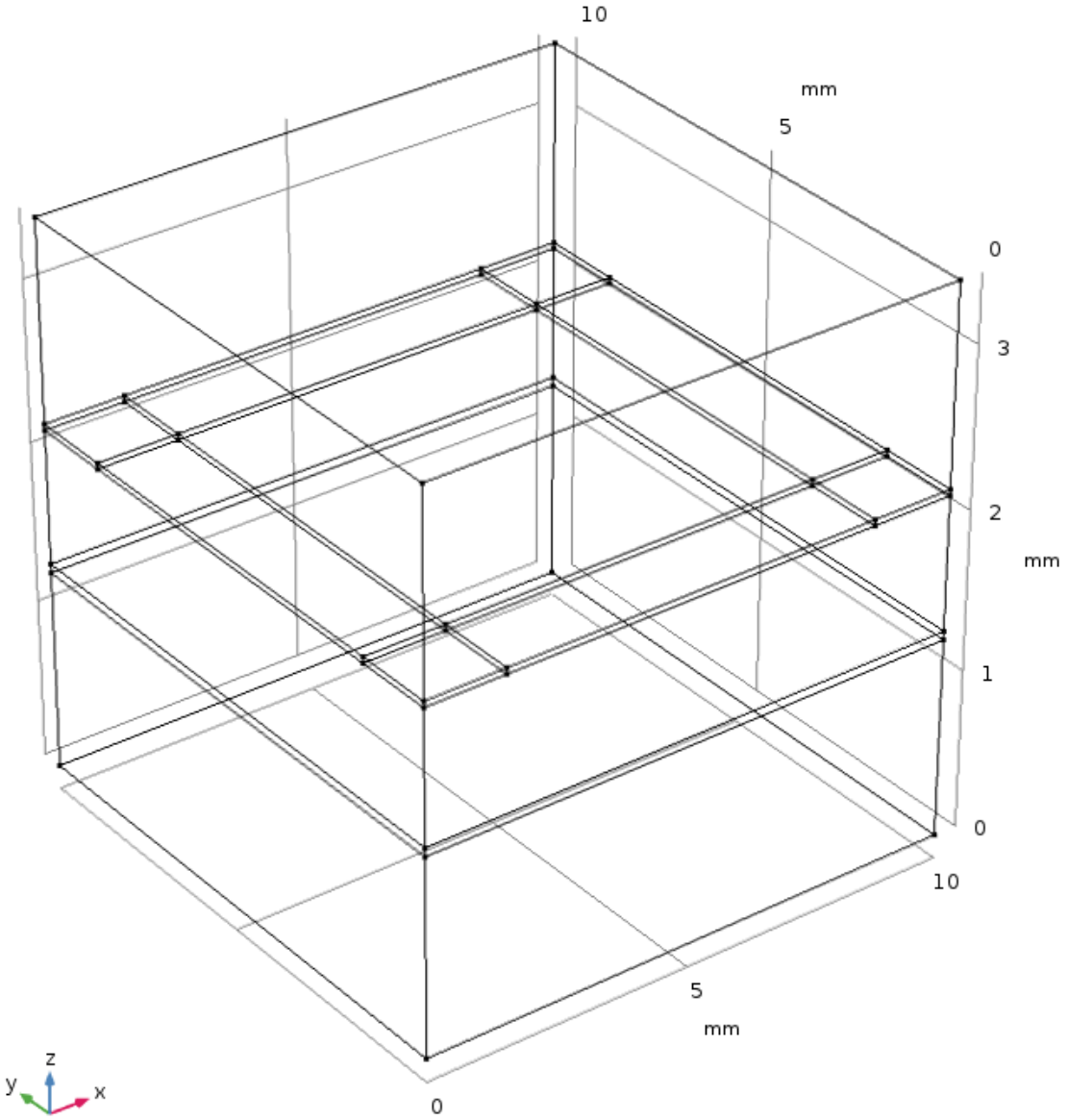

Figure 28. Seven mm COMSOL Unit Cell Model

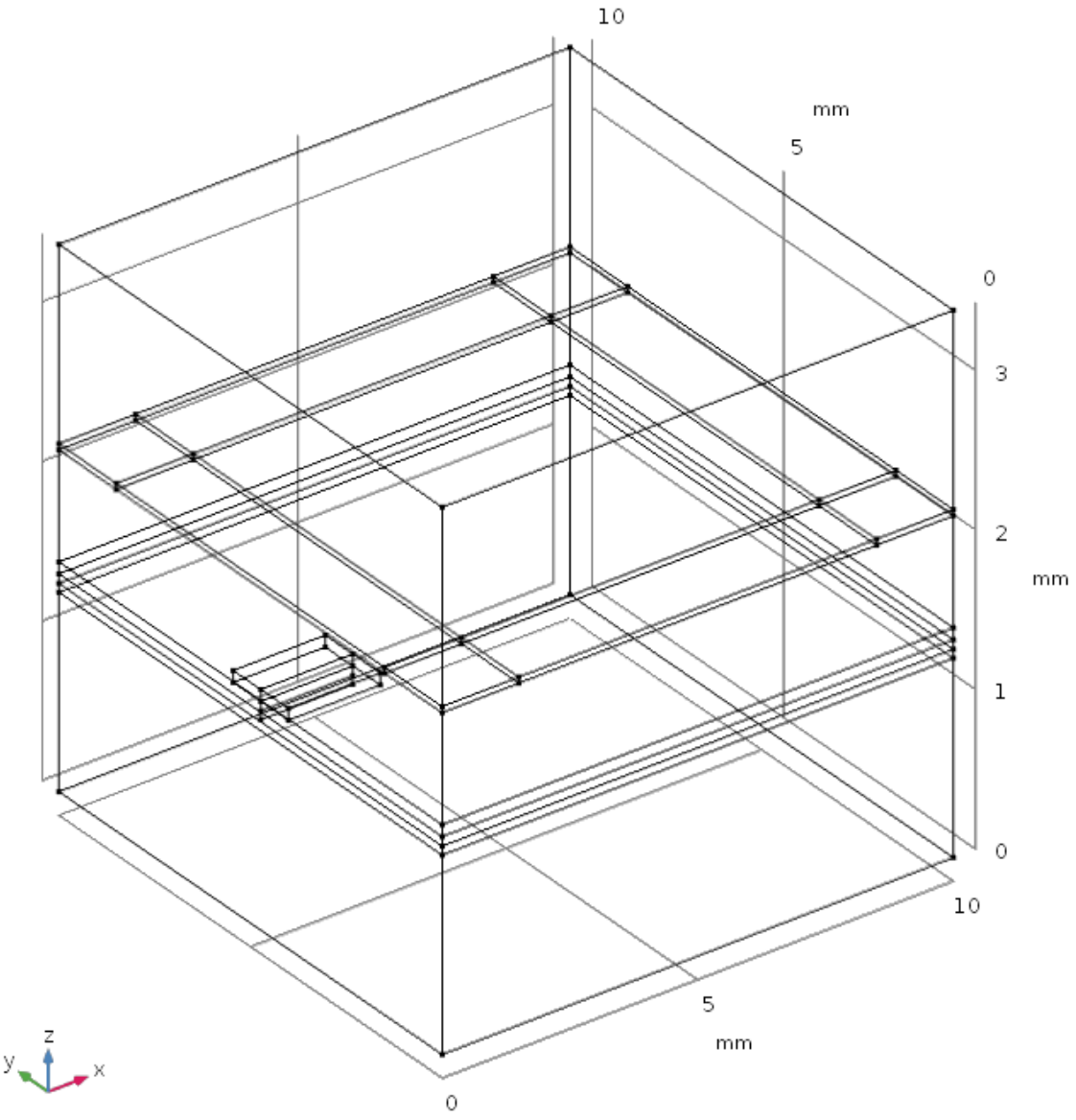

Figure 29. Seven mm COMSOL Unit Cell with Probe and Lumped Port Model

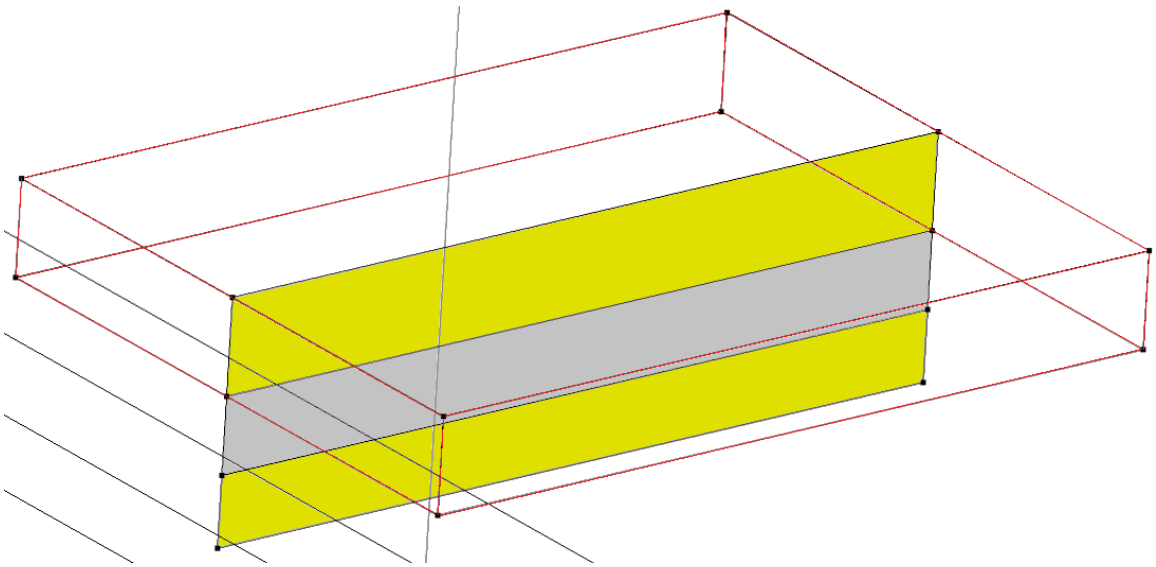

Figure 30. Enlarged Picture of the Probe in Figure 29

Figure 30 is an enlarged view of the probe and Lumped port in Figure 29. The Red rectangle is the lumped port that is in the dielectric material. The gold rectangles are the PECs place between the lumped port located in the probe and ground plane. The gray rectangle is the lumped port located in the dielectric between the probe and ground plane.

THIS PAGE INTENTIONALLY LEFT BLANK

APPENDIX D. SWEEP OSCILLATOR NOTE

Test equipment that generates E&M signals, like the sweep oscillator used for experimental testing, use dBm for the input power. dBm is a base 10 logarithmic power with 1 mW as the reference power. Equation 15 is used to convert a linear power into the logarithmic power. A power of eight watts converts to 39 dBm and a power of two watts converts to 33 dBm.

$$P_{dBm} = 10\log(\frac{P_{linear}}{1\ mW}) \tag{15}$$

THIS PAGE INTENTIONALLY LEFT BLANK

LIST OF REFERENCES

[1] J. Benford, J., Allen, E. Schamilogu, *High Power Microwaves*, 3nd ed., New York, USA, Taylor & Francis Group, 2015.

[2] R. J. Capozzella, "High Power Microwaves on the Future Battlefield: Implications for U.S. Defense," Air War College, Maxwell AFB, USA, 2010.

[3] E. Sedek, R. Slomski, "Overview of Microwave Direct Energy Weapons," in Signal Processing Symposium (SPSympo), IEEE, 2015, pp. 1–3.

[4] R. D. Fisher, "China's Progress with Directed Energy Weapons," International Assessment and Strategy Center, Washington, D.C., 2017.

[5] M. McMahan, "Metamaterial absorbers for microwave detection," M.S. thesis, Phys. Dept., Naval Postgraduate School, Monterey, CA, 2015.

[6] C. H. Hewitt, "Analysis of Broadband Metamaterial Shielding for Counter Directed Energy Weapons," M.S. thesis, Phys. Dept., Naval Postgraduate School, Monterey, CA, 2016.

[7] D. Stoudt, "Naval Directed-Energy Weapons – No Longer a Future Weapon Concept," Naval Surface Warfare Center Dahlgren Division, Dahlgren, VA, USA, 2012.

[8] R. Trim, "A Brief History of the Development of Radar in Great Britain up to 1945," Measurement and Control, vol. 35, no. 10, pp. 299–301, December 2002.

[9] S. D. LeVine, "The Active Denial System: A Revolutionary, Non-Lethal Weapon for Today's Battlefield," Washington, DC, USA, 2009.

[10] B. M. Deveci, "Directed-Energy Weapons: Invisible and Invincible?," M.S. Thesis, Dept. of Information Sciences, Naval Postgraduate School, Monterey, CA, USA, 2007.

[11] M. Backstrom, K. Lovstrand, "Susceptibility of Electron Systems to High-Power Microwaves: Summary of Test Experience," *IEEE Transactions on Electromagnetic Compatibility*, vol. 46, no. 3, pp. 396–403, August 2013.

[12] M. S. Wartak, K. L. Tsakmakidis, O. Hess, "Introduction to Metamaterials," *Physics in Canada*, vol. 67, no. 1, pp. 30–34, January–March 2011.

[13] V. G. Veselago, "The Electrodynamics of Substances with Simultaneously Negative Values of ε and μ," *Soviet Physics Uspekh*, vol. 10, no, 4, pp. 509–514, January–February 1968.

[14] R. A. Shelby, D. R. Smith, S. Schultz, "Experimental Verification of a Negative Index of Refraction," *Science*, vol. 292, no. 5514, pp. 77–79, Apr. 6, 2001.

[15] A. Alu, N. Engheta, "Plasmonic and Metamaterial Cloaking: Physical Mechanisms and Potentials," *Opt. A: Pure Appl. Opt.*, vol. 10, no. 10, p. 093002 (17 pp.), August 2008.

[16] K. Shiraga et al., "Metamaterial Application in Sensing for Living Cells," *Transducers & Eurosensors XXVII: The 17th Conference on Solid_State Sensors, Actuators and Microsystems*, June 2013.

[17] B. Kearney et al., "Al/SiOx/Al single and multiband metamaterial absorbers for terahertz sensor applications," *Optical Eng.*, vol. 52, no. 1, pp. 0138011 – 013801-8, January 2013.

[18] N. Engheta, R. W. Ziolkowski, *Metamaterials Physics and Engineering Exploration*, Hoboken, N.J.: Wiley-Interscience, 2006.

[19] R. S. Kshetrimayum, "A Brief Intro to Metamaterials," *IEEE Potentials*, vol. 23, no. 5, pp. 44–46, December–January 2005.

[20] N. I. Landy et al., "Perfect Metamaterial Absorber," *Physics Review Letters*, vol. 100, no. 20, pp. 207402-1– 207402-4, May 23, 2008.

[21] H. Tao et al., "A Metamaterial Absorber for the Terahertz Regime: Design, Fabrication and Characterization," *Optics Express*, vol. 16, no. 10, pp7181–pp7188, May 12, 2008.

[22] C. M. Watts, X. Liu, W. J. Padilla, "Metamaterial Electromagnetic Wave Absorbers," *Adv. Mater.*, vol. 24, no 23s, OP98-OP120, 2012.

[23] H. Zhai, Z. Li, C. Liang, "A Dual-Band Wide-Angle Polarization-Insensitive Ultrathin Gigahertz Metamaterial Absorber," *Microwave and Optical Technology Letters*, vol. 55, no. 7, pp. 1606–1609, July 2013.

[24] H. A. Atwater, "The Promise of Plasmonics," *Scientific American Special Edition*, vol. 17, no. 3, pp. 56–63, September 2007.

[25] S. O. Kasap, *Principles of Electronic Materials and Devices* 3rd ed., New York, NY, USA: Mcgraw-Hill, ch. 5, 2006.

[26] T. Schubert, E. Kim, *Fundamentals of Electronics Book 1 Electronic Devices and Circuit Applications*, San Rafael, CA, USA: Morgan & Claypool Publishers, ch. 4, pp. 229–278, 2014.

[27] B. T. Kearney, “Enhancing Microbolometer Performance at Terahertz Frequencies with Metamaterial Absorbers,” Dissertation, Phys. Dept., Naval Postgraduate School, Monterey, CA, 2013.

[28] *RF Module User’s Guide*, COMSOL, Los Angeles, CA, USA. 2017.

THIS PAGE INTENTIONALLY LEFT BLANK

INITIAL DISTRIBUTION LIST

1. Defense Technical Information Center
   Ft. Belvoir, Virginia

2. Dudley Knox Library
   Naval Postgraduate School
   Monterey, California